Long-term single-column model intercomparison of diurnal cycle of precipitation over midlatitude and tropical land

Article

Accepted Version

www.reading.ac.uk/centaur

CentAUR

Central Archive at the University of Reading

Reading's research outputs online

Long-Term Single-Column Model Intercomparison on the Diurnal Cycle of Precipitation Over Midlatitude and Tropical Land

Journal:	*QJRMS*
Manuscript ID	QJ-21-0137.R1
Wiley - Manuscript type:	Research Article
Date Submitted by the Author:	n/a
Complete List of Authors:	Tang, Shuaiqi; Pacific Northwest National Laboratory Xie, Shaocheng; Lawrence Livermore National Laboratory Guo, Zhun; Institute of Atmospheric Physics Chinese Academy of Sciences, Climate Change Research Center Hong, Songyou; NOAA Earth System Research Laboratory; CIRES Khouider, Boualem; University of Victoria, Department of Mathematics and Statistics Klocke, Daniel; Deutscher Wetterdienst, Hans Ertel Centre for Weather Research Köhler, Martin; Deutscher Wetterdienst Koo, Myung-Seo; Korea Institute of Atmospheric Prediction Systems Phani, R; Indian Institute of Tropical Meteorology, Monsoon Mission Larson, Vincent; Univ. of Wisconsin -- Milwaukee, Math Sciences Park, Sungsu ; Seoul National University School of Earth and Environmental Sciences Vaillancourt, Paul; Meteorology Research Division, Environment and Climate Change Canada Wang, Yi-Chi; Research Center for Environmental Changes Academia Sinica Yang, Jing; Meteorology Research Division, Environment and Climate Change Canada Daleu, Chimene; University of Reading, Meteorology Homeyer, Cameron; University of Oklahoma, School of Meteorology Jones, Todd; University of Reading, Department of Meteorology Malap, Neelam; Indian Institute of Tropical Meteorology Neggers, Roel; University of Cologne, Institute of Geophysics and Meteorology Prabha, Thara V; Indian Institute of Tropical Meteorology, PM&A Division Ramirez, Enver; National Institute for Space Research Weather Forecast and Climate Studies Centre, Numerical Modeling and Development Division Schumacher, Courtney; Texas A&M University, Department of Atmospheric Sciences Tao, Cheng; Lawrence Livermore National Laboratory Bechtold, Peter; ECMWF Ma, Hsi-Yen; Lawrence Livermore National Laboratory Neelin, David; University of California Los Angeles, Department of Atmospheric and Oceanic Sciences Zeng, Xubin; University of Arizona, Department of Hydrology and

1
2
3
4
5
6
7
8
9
10
11
12
13
14
15
16
17
18
19
20
21
22
23
24
25
26
27
28
29
30
31
32
33
34
35
36
37
38
39
40
41
42
43
44
45
46
47
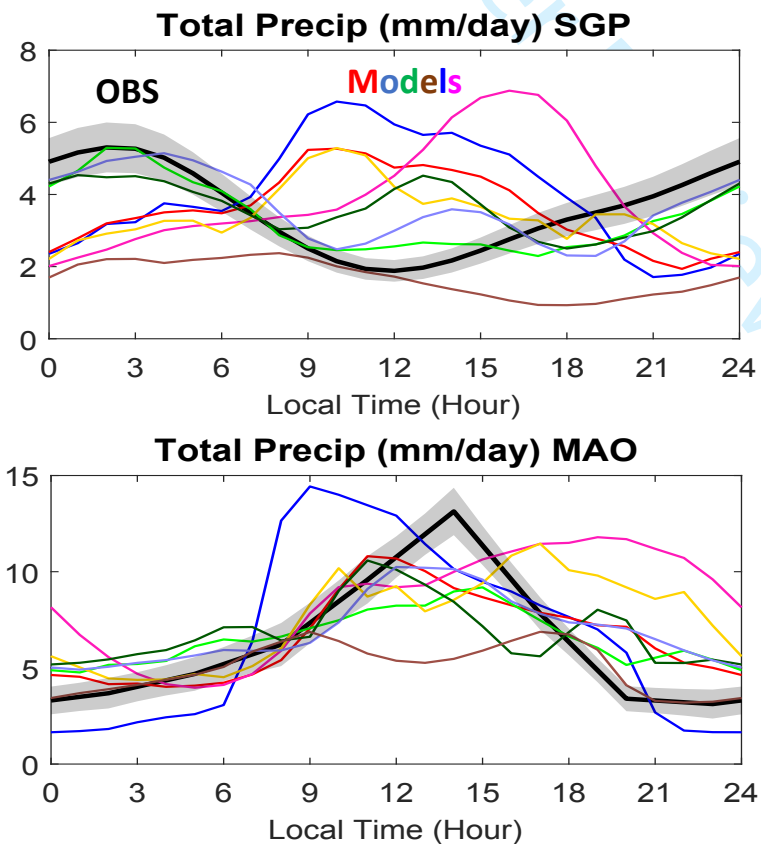48
49
50
51
52
53
54
55
56
57
58
59
60

Long-Term Single-Column Model Intercomparison on the Diurnal Cycle of Precipitation Over Midlatitude and Tropical Land

Shuaiqi Tang, Shaocheng Xie[*], Zhun Guo, Song-You Hong, Boualem Khouider, Daniel Klocke, Martin Köhler, Myung-Seo Koo, Phani Murali Krishna, Vincent E. Larson, Sungsu Park, Paul A. Vaillancourt, Yi-Chi Wang, Jing Yang, Chimene Laure Daleu, Cameron R. Homeyer, Todd R. Jones, Neelam Malap, Roel Neggers, Thara Prabhakaran, Enver Ramirez, Courtney Schumacher, Cheng Tao, Peter Bechtold, Hsi-Yen Ma, J. David Neelin, and Xubin Zeng

Eleven single-column models are used to study the diurnal cycle of precipitation and related physical processes over two continental sites SGP and MAO. Most models produce afternoon precipitation too early, likely due to the missing transition of shallow-to-deep convection in the models. Many models cannot produce convection occurring at nighttime. Unified treatment of shallow and deep convection and the capability to capture mid-level convection are important for models to capture diurnal cycle of precipitation.

Long-Term Single-Column Model Intercomparison on the Diurnal Cycle of Precipitation Over Midlatitude and Tropical Land

Shuaiqi Tang[1], Shaocheng Xie[2*], Zhun Guo[3], Song-You Hong[4], Boualem Khouider[5], Daniel Klocke[6#], Martin Köhler[7], Myung-Seo Koo[8], Phani Murali Krishna[9], Vincent E. Larson[10,1], Sungsu Park[11], Paul A. Vaillancourt[12], Yi-Chi Wang[13], Jing Yang[12], Chimene Laure Daleu[14], Cameron R. Homeyer[15], Todd R. Jones[14], Neelam Malap[9], Roel Neggers[16], Thara Prabhakaran[9], Enver Ramirez[17], Courtney Schumacher[18], Cheng Tao[2], Peter Bechtold[19], Hsi-Yen Ma[2], J. David Neelin[20], and Xubin Zeng[21]

1. Pacific Northwest National Laboratory, Richland, WA, USA

2. Lawrence Livermore National Laboratory, Livermore, CA, USA

3. Climate Change Research Center, Institute of Atmospheric Physics, Chinese Academy of Sciences, Beijing, China.

4. NOAA/Earth System Research Laboratory and CIRES/University of Colorado, Boulder, CO, USA

5. Department of Mathematics and Statistics, University of Victoria, Victoria, BC, Canada

6. Hans Ertel Centre for Weather Research, Deutscher Wetterdienst, Offenbach, Germany

7. Deutscher Wetterdienst, Offenbach, Germany

8. Korea Institute of Atmospheric Prediction Systems, Seoul, South Korea

9. Indian Institute of Tropical Meteorology, Pune, India

10. Department of Mathematical Sciences, University of Wisconsin-Milwaukee, Milwaukee, WI, USA

11. School of Earth and Environmental Sciences, Seoul National University, Seoul, South Korea

12. Meteorology Research Division, Environment and Climate Change Canada, Dorval, Québec, Canada

13. Research Center for Environmental Changes, Academia Sinica, Taipei, Taiwan

14. Department of Meteorology, University of Reading, Reading, UK.

15. School of Meteorology, University of Oklahoma, Norman, OK, USA

16. Institute of Geophysics and Meteorology, University of Cologne, Cologne, Germany

17. Numerical Modeling and Development Division, Center for Weather Forecasting and Climate Studies, National Institute for Space Research, São Paulo, Brazil

18. Department of Atmospheric Sciences, Texas A&M University, College Station, TX, USA

37   19. European Centre for Medium-Range Weather Forecasts, Reading, UK

38   20. Dept. of Atmospheric and Oceanic Sciences, University of California in Los Angeles,
39   Los Angeles, CA, USA

40   21. Department of Hydrology and Atmospheric Sciences, University of Arizona, Tucson,
41   AZ, USA

42

43   # now at Max-Planck-Institut für Meteorologie, Hamburg, Germany

44

45

46

47

48

49

50

51

52

53

54

55

56   Contact: Shaocheng Xie (xie2@llnl.gov)

57

1
2
3
4
5
6
7
8
9
10
11
12
13
14
15
16
17
18
19
20
21
22
23
24
25
26
27
28
29
30
31
32
33
34
35
36
37
38
39
40
41
42
43
44
45
46
47
48
49
50
51
52
53
54
55
56
57
58
59
60

58   Abstract

59   General Circulation Models (GCMs) have for decades exhibited difficulties in modeling the

60   diurnal cycle of precipitation (DCP). This issue can be related to inappropriate representation of

61   the processes controlling sub-diurnal phenomena like convection. In this study, eleven single-

62   column versions of GCMs are used to investigate the interactions between convection and

63   environmental conditions, processes that control nocturnal convections, and the transition from

64   shallow to deep convection on diurnal time scale. Long-term simulations are performed over two

65   continental land sites: the Southern Great Plains (SGP) in the U.S. for twelve summer months

66   from 2004 to 2015 and the Manacapuru site at the central Amazon (MAO) in Brazil for two full

67   years from 2014 to 2015. The analysis is done on two regimes: afternoon convective regime and

68   nocturnal precipitation regime. Most models produce afternoon precipitation too early, likely due

69   to the missing transition of shallow-to-deep convection in these models. At SGP, the unified

70   convection schemes better simulate the onset time of precipitation. At MAO, models produce

71   heating peak in a much lower level comparing with observation, indicating too shallow

72   convection in the models. For nocturnal precipitation, models that produce most of nocturnal

73   precipitation all allow convection to be triggered above the boundary layer. This indicates the

74   importance of model capability to detect elevated convection for simulating nocturnal

75   precipitation. Sensitivity studies indicate that (1) nudging environmental variables towards

76   observations has a minor impact on the diurnal cycle of precipitation; (2) unified treatment of

77   shallow and deep convection and the capability to capture mid-level convection are important for

78   models to capture DCP; and (3) the interactions of the atmosphere with other components in the

79   climate system (e.g., land) are also important for DCP simulations in coupled models. These

80   results provide long-term statistical insights on which physical processes are essential in climate

81   models to simulate DCP.

82

1. Introduction

The diurnal cycle of precipitation (DCP) is one of the most important signals affecting climate variability and weather forecasting. Although it is dominated by diurnal variation of solar insolation that greatly affects the surface energy budget and regulates surface temperature (Dai et al. 1999), mesoscale propagating systems and large scale envelopes are also responsible to regulate the DCP (e.g., Rutledge and Hobbs 1984; Wei et al. 2020). As a benchmark for evaluating climate models (Covey et al. 2016), DCP provides an excellent measure of how well climate models simulate not only the total amount of precipitation but also its frequency, intensity, timing and duration (Trenberth et al. 2003).

General Circulation Models (GCMs) have for decades exhibited difficulties in modeling the diurnal precipitation. Dai (2006) examined 18 GCMs and found that many models showed peak precipitation around noontime over land and around 02 local standard time (LST) over ocean, both a few hours earlier than observations. Covey et al. (2016) examined 24 models from phase 5 of the Coupled Model Intercomparison Project (CMIP5, Taylor et al. 2012), and found similar biases; i.e. GCMs produce warm season rainfall too early in the day. Recently, Fiedler et al. (2020) and Tang et al. (2021) examined the latest GCMs from CMIP6 (Eyring et al. 2016) compared with earlier CMIP versions. They found that although CMIP6 models have made improvements on DCP, they still suffer from the same problems: producing rainfall too early in the day over land and missing nocturnal rainfall peak associated with elevated convection and propagating mesoscale convective systems (MCSs).

These issues in simulating DCP in climate models can be related to inappropriate representation of the processes that control sub-diurnal phenomena like convection, and phenomena with timescales of several hours, like MCSs. Many studies attribute the model biases on DCP to the deficiencies in convective parameterizations (e.g., Koo and Hong 2010). Great efforts have been made to improve DCP in GCMs by improving the convective trigger (e.g., Xie and Zhang 2000; Bechtold et al. 2004; Rio et al. 2009; Wang and Hsu 2019; Xie et al. 2019), closure (e.g., Zhang 2003; Rio et al. 2009; Bechtold et al. 2014), entrainment and detrainment rates (e.g., Wang et al. 2007; Bechtold et al. 2008; Stratton and Stirling 2012), or the detection of mid-level convection that is related to the nocturnal precipitation peak over regions such as the central U.S. (e.g., Lee et al. 2008; Wang et al. 2015; Xie et al. 2019; McTaggart-Cowan et al. 2020). Other parameterizations (e.g., Park 2014a, 2014b; Neggers 2015a; Guo et al. 2021) that unify the deep convective scheme with other parameterizations also provide a path toward improving DCP simulation. The effort of unifying the representation of subgrid-scale convection in GCMs has a long history. One of the serious challenges is that our knowledge of convective physics and dynamics, in particular the limits of applicability of parametric relations that capture observed behavior, is still very limited. This lack of insight is driving intense research into convective transitions, including various recent meteorological field campaigns dedicated to this problem (e.g., CACTI, Varble et al. 2021).

121 A single-column model (SCM) is a useful tool to test physical processes within a column of a
122 GCM (Randall et al. 1996; Zhang et al. 2016; Lin and Xie 2021). In the past twenty years,
123 several SCM intercomparison studies have been organized, focusing on summertime continental
124 convection (Ghan et al. 2000; Xie et al. 2002; Guichard et al. 2004), springtime midlatitude
125 frontal clouds (Xie et al. 2005; Xu et al. 2005), shallow-cumulus clouds over mid-latitude land
126 (Lenderink et al. 2004), marine stratocumulus-topped boundary layers (Bretherton et al. 1999;
127 Zhu et al. 2005; Wyant et al. 2007; Neggers et al. 2017), mixed-phase clouds in the polar region
128 (Klein et al. 2009; Morrison et al. 2009; Pithan et al. 2016) and deep convection over the tropical
129 ocean (Bechtold et al. 2000; Davies et al. 2013; Petch et al. 2014). These intercomparison studies
130 serve as testbeds for developing new parameterizations. For DCP, SCMs produce a similar
131 diurnal structure of precipitation as the full 3-D GCM and are thus suitable to be used as a
132 simplified model of GCMs to explore the physical processes related to DCP (Betts and Jakob
133 2002).

134 The above-mentioned SCM intercomparison studies mainly focused on case studies. In recent
135 years efforts have been made to pursue longer-term SCM simulations at permanent
136 meteorological sites (Neggers et al. 2012). In certain conditions this allows direct attribution of
137 persistent biases in GCMs to parameterized subgrid-scale processes (Neggers and Siebesma
138 2013; Neggers 2015b). In the recent Global Atmospheric System Studies (GASS) Diurnal Cycle
139 of Precipitation intercomparison project (https://portal.nersc.gov/project/capt/diurnal/), we are
140 attempting to build robust statistics of the diurnal cycle of precipitation using long-term
141 simulations from various weather and climate models. Two research sites from the Atmospheric
142 Radiation Measurement (ARM) program, Southern Great Plains (SGP) site in the central U.S.
143 and the Manacapuru (MAO) site for the Green Ocean (GoAmazon2014/5, Martin et al. 2016)
144 experiment in Brazil, are chosen to build the long-term statistics of SCM performance. In
145 addition, a few 1-day cases are selected to use both SCMs and cloud-resolving models (CRMs)
146 for detailed process understanding of model errors in DCP. The goal of this study is to document
147 common model behaviors in simulating the diurnal cycle of precipitation in current weather and
148 climate models by constraining the large-scale conditions in the SCM framework and to provide
149 a benchmark for more in-depth follow-up studies. In particular, this paper will focus on the long-
150 term statistics of the SCM simulations on DCP. More results on SCMs and CRMs for selected
151 cases will be analyzed in a separate paper.

152

2.   Experimental Design and Participating Models

154

2.1 Experimental Design

156 Two sets of SCM experiments are designed to build up statistics and connection to climate errors
157 at two continental land locations using a series of short-range 5-day hindcast simulations. The
158 first experiment spans twelve warm seasons (May – August) between 2004 to 2015 at the ARM

159 SGP site. The second experiment is two full years from 2014 to 2015 at the ARM MAO site. The

160 default protocol for the SCM simulations is a 5-day non-nudging hindcast, i.e., each SCM is

161 initiated at 00Z every day and runs freely for 5 days without constraining temperature and

162 moisture fields. Compared to typical SCM experiment protocols such as free run (e.g., Ghan et

163 al. 2000) or nudging run, in the hindcast run the large-scale condition will not drift too far away,

164 and the SCM is expected to replicate similar model biases as in GCM (Bogenschutz et al. 2020),

165 so that modelers can identify problems related to parameterizations using SCM hindcast run. In

166 this study, the 24 – 48 hr simulations (day-2 hindcast) are used for analysis. In total there are 123

167 days (1 May to 31 August) per warm season at SGP and 361 days (2 January to 28 December

168 since the 5-day simulations do not cross two years) per year at MAO to build the statistics.

169 SCMs are driven with the large-scale forcing derived from the constrained variational analysis

170 (Zhang and Lin 1997; Zhang et al. 2001), which has been widely used in earlier GASS SCM

171 intercomparison studies. The large-scale forcing data at SGP are from the ARM continuous

172 forcing datasets at SGP (Xie et al. 2004; Tang et al. 2019), while the large-scale forcing at MAO

173 are described in Tang et al. (2016). The initial conditions, surface latent and sensible heat fluxes,

174 horizontal winds and the large-scale horizontal and vertical advections are all prescribed from

175 the large-scale forcing data. Precipitation in the large-scale forcing data, which are from radar

176 measurements averaged within a domain of ~300km in diameter at SGP and ~220km in diameter

177 at MAO, is also used to evaluate model performance.

178 2.2 Participating Models

179 Participants in this intercomparison project submitted results from 11 SCMs with all required

180 simulations at SGP and MAO. The basic information of these models is listed in Table 1, and

181 more information about their deep convective parameterizations is listed in Table 2. Note that

182 some of these models have an inheritance relationship with differences in model versions or

183 physical parameterizations. For example, EAMv1 has two other versions: EAMv1.trigger and

184 EAMv1.SILHS, with different deep convective schemes. EAMv1.trigger applies a modified

185 convective trigger that was shown to significantly improve DCP (Xie et al. 2019);

186 EAMv1.SILHS shuts off EAMv1's native deep convective scheme and lets the Cloud Layers

187 Unified By Binormals scheme (CLUBB) treat both shallow and deep convection (Thayer-Calder

188 et al. 2015; Guo et al. 2021), with a Subgrid Importance Latin Hypercube Sampler (SILHS,

189 Larson and Schanen 2013) to interface clouds with microphysics on the subgrid scale. Moreover,

190 SCAM5 is the earlier version of SCAM6, and SAM0-UNICON is developed based on SCAM5

191 with a unified convection scheme (UNICON, Park 2014a, 2014b) for shallow and deep

192 convection. Some models also perform simulations with different model setups or configurations

193 for sensitivity studies. For example, SCAM6 and SKIM perform simulations with an interactive

194 land model; SKIM submitted simulations with atmospheric states nudging to the observations.

195 The variety of simulations allows us to test model sensitivity to parameterizations and model

196 setup. Although models have different vertical and temporal resolution, they are all interpolated

197   (or averaged) into 40 vertical levels and 1-hour resolution. The model data are archived and
198   publicly available at https://portal.nersc.gov/project/mp193/GASS/SCM/data/.

199

3.   Model Performances on the Mean Diurnal Cycle of Precipitation

201

202   3.1 General features

203   The two ARM sites are located in two distinct but representative environmental conditions: SGP
204   represents typical mid-latitude land condition with upper-level westerlies and dry free
205   troposphere; MAO represents typical tropical rain-forest conditions with warm, moist air in the
206   lower and middle troposphere. A set of diagnostic plots of the meteorological and process-level
207   variables are made available at the GASS-DCP quick-plot webpage
208   (https://portal.nersc.gov/project/mp193/GASS/SCM/quick_plots/). Due to the length limit, this
209   paper only shows some of them that are closely related to DCP.

210   The mean DCP and the harmonic dial plots for the twelve summer seasons at SGP and the two
211   years at MAO are shown in Figure 1. "Harmonic dial plot" (Covey et al. 2016) is a two-
212   dimensional vector diagram in which the radius and angle represent the amplitude and phase,
213   respectively, of the first component of Fourier analysis on the diurnal timeseries (sinusoidal
214   function with period of 24 hours). The observed precipitation at SGP shows a nocturnal
215   precipitation peak after midnight and a daytime minimum at around noon. The diurnal harmonic
216   peak is at around 01 LST. Many models, such as EAMv1, SCAM6, SAM0-UNICON and
217   SMCPCP, produce a precipitation peak during daytime, with harmonic phases between ~11 and
218   15 LST and amplitudes between 1 and 2 mm/day. The failure to produce a nocturnal
219   precipitation peak at SGP is consistent with previous global model studies (e.g., Tang et al.
220   2021). ICON produces early-morning precipitation peak but its magnitude and diurnal amplitude
221   are much lower than the observations. A few models produce a nocturnal precipitation peak,
222   such as SKIM, CMC and TaiESM1. The mechanisms that help these models capturing nocturnal
223   precipitation will be discussed later in Section 3.3.

224   The observed precipitation at MAO shows an early afternoon peak with the diurnal harmonic
225   peak just after noon. The precipitation peak is stronger and smoother in the wet season, while it
226   is weaker and sharper in the dry season (Figure 2). Models have a spread in diurnal amplitude
227   and phase, with precipitation amplitudes ranging from 1.5 to 6 mm/day and the diurnal phases
228   occurring as early as 12 LST to as late as 17 LST. The diurnal phases in both observations and
229   models are more similar in the dry season than in the wet season, while the precipitation amounts
230   and amplitudes are larger in the wet season for observation and most models (Figure 2). Since
231   DCP is affected by several types of convective systems that occur at different times of the day in
232   both dry and wet seasons (e.g., Tang et al. 2016), we will focus on model performance for
233   different types of convective systems instead of in different seasons.

234   The observed cloud fractions at SGP and MAO both show a low-level cloud peak rising along
235   with the daytime boundary layer development (Figure 3). The transition of shallow-to-deep
236   convection has been extensively studied focusing on the following mechanisms: boundary layer
237   turbulence strength, including boundary layer inhomogeneity (e.g., Zhang and Klein 2010) and
238   cold pools from rain evaporation (e.g., Khairoutdinov and Randall 2006; Mapes and Neale 2011;
239   Del Genio et al. 2012); and free troposphere humidity and instability, including the
240   preconditioning from shallow convection via detrainment or dilution (e.g., Rio et al. 2009;
241   Mapes and Neale 2011; Del Genio et al. 2012; de Rooy et al. 2013; Hohenegger and Stevens
242   2013; Ruppert and Johnson 2015; Zermeño-Díaz et al. 2015). Most of these studies used
243   observations or idealized models, and only a few of them attempted to represent the transition in
244   GCMs (e.g., Rio et al. 2009; Del Genio et al. 2012). Among the eight SCMs, SAM0-UNICON
245   well captures the gradually rising of low clouds peak at both SGP and MAO; EAMv1 and
246   SCAM6 capture the low clouds rising, although their low cloud fraction is underestimated at
247   SGP; other models all fail to produce the rising low clouds in the daytime. This result reveals the
248   importance of unifying turbulence and shallow convective scheme (CLUBB) or shallow and
249   deep convective scheme (UNICON) in simulating the development of shallow clouds and the
250   transition from shallow to deep clouds. This is consistent with the findings in previous attempts
251   of unified schemes such as in Frenkel et al. (2011a, 2011b), which used a simple multicloud
252   model coupled to a bulk boundary layer scheme to simulate the diurnal cycle of tropical
253   precipitation. For high clouds, most models overestimate high cloud fraction comparing to
254   observations at SGP and MAO. The diurnal variation of high clouds is also poorly simulated at
255   SGP but reasonably reproduced at MAO. The different model performances in different
256   locations indicate the complexity to develop globally uniform parameterizations.

257   Previous studies have shown a relationship between precipitation and column-integrated relative
258   humidity (CRH) in observations at daily (e.g., Bretherton et al. 2004) and sub-daily (e.g.,
259   Holloway and Neelin 2009; Neelin et al. 2009) timescales, although it should be noted that using
260   CRH is an approximation for a more complex precipitation-moisture-temperature relationship
261   (Kuo et al. 2018). How well models can capture the observed precipitation-CRH relationship is
262   related to the representation of convection and its interaction with the large-scale environment
263   and provides insights to model improvements on convection and precipitation (e.g., Kuo et al.
264   2020). Here we also examine the relationship of precipitation amount and frequency with CRH,
265   as well as the occurrence frequency of each CRH bin (2% interval) in Figure 4. Observations
266   show a strongly increasing relationship between precipitation amount and CRH at both sites.
267   Precipitation picks up quickly and increases exponentially when CRH reaches 60% ~ 70% at
268   SGP and 75% ~ 80% at MAO. Most models, except ICON, simulate higher (lower) precipitation
269   probability (Figure 4 mid-row) and precipitation amount (Figure 4 top-row) compared to the
270   observations when CRH is low (high). However, there are also more high-CRH days and less
271   moderate-CRH days in these models than in observations (Figure 4 bottom-row). This indicates
272   that models tend to produce light rainfall too easily in moderately dry conditions but have
273   difficulties producing strong precipitation in wet conditions, although they are more likely to

274 produce high CRH. This is consistent with the long-standing model error in GCMs that models
275 rain too frequently at reduced intensity (Dai 2006; Sun et al. 2007; Stephens et al. 2010). In
276 ICON, precipitation picks up at a much higher CRH. It also produces more wet conditions and
277 less dry conditions than observations and other models. This may be related to the fact that
278 ICON requires the whole box to be saturated for large-scale precipitation while other models
279 allow partial cloudiness for microphysics. This would lead to a later onset of large-scale
280 precipitation and higher relative humidity in ICON.

281 In the next two subsections, we select two convection regimes to further investigate the model
282 biases on DCP: afternoon precipitation regime that is primarily surface-driven deep convection
283 and nocturnal precipitation regime that is primarily associated with propagating MCSs and
284 elevated convection. Based on observations, the afternoon precipitation days are selected by
285 modifying the criteria of Zhang and Klein (2010). For SGP, an afternoon precipitation day is
286 chosen when it has (1) peak rain rate greater than 1 mm/day, (2) rain peak time between 13 and
287 20 LST and (3) the peak rain rate 1.5 times greater than any rain rate outside of 13 to 20 LST.
288 For MAO, an afternoon precipitation day is chosen when it has (1) peak rain rate greater than 1
289 mm/day, (2) rain peak time between 11 and 20 LST, (3) the peak rain rate 1.5 times greater than
290 any rain rate outside of 11 to 20 LST, and (4) it must fall into the locally-driven convection case
291 library visually selected from radar and satellite images (Tian et al. 2021). The last criterion is set
292 to exclude those cases of propagating MCSs with a daytime rainfall peak, which occur frequently
293 during the rainy season at MAO and overlap with locally generated rainfall (Tang et al. 2016). A
294 nocturnal precipitation day at SGP and MAO is chosen when it has (1) peak rain rate greater than
295 1 mm/day, and (2) rain peak time between 00 and 07 LST. Overall, there are 136 and 380 days
296 selected for the afternoon and nocturnal precipitation days, respectively, during the twelve warm
297 seasons at SGP, and 111 and 73 days selected for the afternoon and nocturnal precipitation days,
298 respectively, during the two years at MAO.

299   3.2 Afternoon Precipitation Regime

300 The mean diurnal cycle of total precipitation and convective precipitation fraction for the
301 selected afternoon precipitation days at SGP and MAO are shown in Figure 5. Also shown are
302 the harmonic dial plots of total precipitation. The observations show that the afternoon regime
303 precipitation picks up after 09 LST at both sites, reaches a daily maximum around 17 LST at
304 SGP and 14 LST at MAO, then decreases to late-night/early-morning values around 21 LST. In
305 the diurnal harmonic analysis, the diurnal phase of afternoon precipitation at SGP is well
306 captured in most SCMs, as opposed to the timeseries of all events in Figure 1, while their diurnal
307 amplitudes vary. At MAO, models have a large spread of afternoon precipitation peak time,
308 consistent with the timeseries of all events in Figure 1. EAMv1 shows large precipitation in the
309 morning with the diurnal phase peak at noon; SMCPCP and SAM0-UNICON have a late
310 afternoon peak just after 18 LST; SCAM6, SKIM and TaiESM1 capture the observed diurnal
311 phase, but their diurnal amplitudes are much smaller. ICON produces two precipitation peaks,
312 one in the morning and the other in the late afternoon, with much lower magnitude. The different

313   model treatments of the preconditioning, triggering, developing of convection and convection

314   interaction with environment via entrainment/detrainment may be responsible for the large

315   spread or model performance. Another aspect is the presence of cold pool environments and

316   associated boundary layer features and triggering of secondary developments, leading to the

317   propagation as well as organization of convection (e.g., Oliveira et al. 2020). It is also likely that

318   these processes are complex and location-dependent, so that effort is needed to improve the

319   current globally uniform convective parameterization.

320   Figure 6 shows the frequency of diurnal maximum precipitation occurrence at each hour. The

321   model performance of maximum precipitation frequency is consistent with their performance of

322   mean DCP in Figure 5. The maximum diurnal precipitation occurs mostly between 15 – 19 LST

323   at SGP and 13 – 17 LST at MAO, consistent with the time of large mean diurnal precipitation

324   (Figure 5). Models generally capture the maximum precipitation time at SGP, with a few

325   percentages of time when models produce maximum precipitation too early or too late. At MAO,

326   models frequently produce maximum precipitation either too early or too late compared to

327   observation, except SKIM. This again indicates that the response of model precipitation to

328   environment at moist tropical land is not as sophisticated as at mid-latitude land.

329   In the daytime, all models produce most of their precipitation from convection, with convective

330   precipitation fraction close to 100% (second row of Figure 5). The model performance of

331   afternoon convection is further examined by looking at the vertical profiles of apparent heating

332   (Q_1) and drying (Q_2) in Figure 7. Q_1 and Q_2 were first introduced by Yanai et al. (1973) to

333   estimate the diabatic processes:

334
$$Q_1 = \frac{1}{C_p}\left(\frac{\partial \bar{s}}{\partial t} + \overline{\vec{V}} \cdot \nabla \bar{s} + \bar{\omega}\frac{\partial \bar{s}}{\partial p}\right) = \frac{1}{C_p}\left(Q_{rad} + L_v(d_w + d_i) - \frac{\partial \overline{\omega's'}}{\partial p}\right) \qquad (1)$$

335
$$Q_2 = -\frac{L_v}{C_p}\left(\frac{\partial \bar{q}}{\partial t} + \overline{\vec{V}} \cdot \nabla \bar{q} + \bar{\omega}\frac{\partial \bar{q}}{\partial p}\right) = \frac{L_v}{C_p}\left(d_w + d_i + \frac{\partial \overline{\omega'q'}}{\partial p}\right) \qquad (2)$$

336   where $s = C_p T + gz$ is the dry static energy and C_p is the specific heat for dry air in constant

337   pressure; q is water vapor mixing ratio; $\vec{V}$ is horizontal wind vector; ω is vertical velocity in

338   pressure coordinate; Q_{rad} is radiative heating; $L_v(d_w + d_i)$ is the latent heat from liquid and ice

339   processes; the overbar refers to a horizontal average and the prime refers to a deviation from the

340   average. The "observed" Q_1 and Q_2 are derived from the large-scale dynamics (the center part of

341   the equations) from the variational analysis while the "simulated" Q_1 and Q_2 are the sum of all

342   physical tendencies in the model (the right-hand-side of the equations). The simulated vertical

343   profiles of Q_1 and Q_2 are generally consistent with observations at SGP (Figure 7, left column),

344   with heating peak in the middle to upper troposphere around 400 to 500 hPa. However, there are

345   large discrepancies of Q_1 and Q_2 profiles at MAO (Figure 7, right column). Models produce a

346   heating peak near 700 to 800 hPa, much lower than the observed peak at near 500 hPa. While the

347   observed heating remains large to about 150 mb, model heating is small about 500 mb. They also

348   fail to reproduce the observed moisture sink between 250 and 650 hPa. These discrepancies were

1
2
3
4
5
6
7
8
9
10
11
12
13
14
15
16
17
18
19
20
21
22
23
24
25
26
27
28
29
30
31
32
33
34
35
36
37
38
39
40
41
42
43
44
45
46
47
48
49
50
51
52
53
54
55
56
57
58
59
60

349 also found in Large Scale Biosphere–Atmosphere Experiment (LBA) conducted in Southwest
350 Amazonia (Ma et al. 2021a), indicating that models produce too shallow afternoon convection
351 over the broad Amazon region. The fact that models simulate Q_1 and Q_2 well at SGP but poorly
352 at MAO also highlights the dependence of model performances at different locations. The poor
353 performance at deep convection at MAO despite being driven by observed large-scale forcing
354 suggests significant common deficiencies in deep convective parameterization over tropical land.

355 At both SGP and MAO, a common model bias in DCP is the early onset of precipitation. The
356 observed diurnal precipitation at both SGP and MAO picks up quickly near 12 LST, while many
357 models produce notable precipitation a few hours earlier (Figure 5). To further quantify the early
358 onset of precipitation, we define the precipitation onset time as the first hour after 06 LST when
359 the precipitation at that hour increases above 1 mm/day. The statistics of precipitation onset time
360 are shown in Figure 8. The models we are discussing in this section are shown in thick lines, and
361 those will be discussed in Section 4 for sensitivity study are shown in thin lines. The mean onset
362 time of precipitation is observed in early afternoon at SGP and around noon at MAO, about 3-4
363 hours earlier than the maximum precipitation time (Figure 6). However, the SCM-simulated
364 onset time is usually 1 to 2 hours earlier than in observations at SGP, and up to 4 hours earlier at
365 MAO, even for those models produce maximum precipitation in a later time (Figure 6). CMC
366 and ICON have a consistent mean precipitation onset time with observation at MAO, but their
367 diurnal distribution is broader, with three (CMC) or two (ICON) precipitation peaks during the
368 daytime (top right panel of Figure 5).

369 Among these SCMs, EAMv1, SCAM6, SMCPCP and ICON use CAPE to trigger deep
370 convection (Table 2). This CAPE-based convective trigger is believed to trigger convection too
371 easily and too frequently (e.g., Xie and Zhang 2000; Ma et al. 2021b). A modified trigger using
372 dynamic CAPE (dCAPE) introduced by Xie and Zhang (2000) and further enhanced in Xie et al.
373 (2019) is implemented in EAMv1.trigger and show promising results on mitigating the early
374 onset of convection (see further discussion in Section 4). Using a CIN-based convective trigger,
375 SKIM shows good precipitation onset time at SGP, but too early onset time at MAO, possibly
376 due to the low-CIN environment in the Amazon permitting convection to trigger too easily but
377 not through a sufficient deep layer.

378 Another well-known issue of early onset of deep convection in GCMs is the poor simulation of
379 the transition of shallow-to-deep convection and the gradual moistening of the free troposphere
380 (Guichard et al. 2004; Zhang and Klein 2010). Shallow and deep convection is usually related to
381 very different forcing regimes, entrainment and detrainment rates, and environment conditions.
382 Therefore, almost all previous GCMs separate them into different schemes, and they work
383 reasonably well in practice. However, separating the two schemes usually leads to an overly
384 abrupt transition from one condition to another (e.g., Rio et al. 2009). Deep convection is often
385 triggered as soon as the large-scale environment reaches the triggering criterion in the model,
386 instead of developing through an intermittent stage of preconditioning of the free atmosphere as
387 in the real world. SAM0-UNICON uses a new parameterization that aims to unify shallow and

388 deep convective schemes to simulate the complex interactions between subgrid and grid-scale
389 processes such as the transition from shallow to deep convection. While it correctly simulates the
390 precipitation onset time at SGP, at MAO in encounters similar deficiency of ~2 hr earlier onset
391 time (Figure 8). It may be partly related with the inability of SCM to handle horizontal advection
392 of subgrid cold pool that is parameterized within UNICON. This reveals a major challenge in
393 unified parameterization to treat all conditions within a single set of equations and a need to test
394 the models in global simulations.

395   3.3 Nocturnal Precipitation Regime

396 The mean diurnal cycle of total precipitation, convective precipitation fraction and the diurnal
397 harmonic dial plots of total precipitation for nocturnal precipitation days are shown in Figure 9.
398 Nocturnal precipitation is typically related to the elevated convection above nocturnal stable
399 boundary layer (e.g., Lee et al. 2008; Geerts et al. 2017) or propagating MCSs. The observations
400 show a diurnal peak at ~03 LST at SGP and ~05 LST at MAO, with a diurnal peak of ~20
401 mm/day and harmonic amplitude of ~8 mm/day, much larger than the afternoon precipitation
402 events in Figure 5. At 12~15 LST, precipitation at SGP reaches its diurnal minimum, while
403 precipitation at MAO reaches a secondary peak, close to but, weaker than the peak of afternoon
404 precipitation. This indicates that even when the nocturnal precipitation has released some
405 instability of the atmosphere, the solar heating in the following daytime and the moist
406 environment can still trigger afternoon convection.

407 From Figure 9, SCMs can be divided into two groups in simulating nocturnal precipitation at
408 SGP. SKIM, CMC and TaiESM1 well capture the diurnal phase and amplitude of nocturnal
409 precipitation, and ICON also captures the diurnal phase but underestimates the amplitude of
410 nocturnal precipitation. EAMv1, SCAM6, SAM0-UNICON and SMCPCP produce diurnal
411 precipitation later with smaller magnitude. At MAO, the four "good" models also perform well,
412 while the other models produce either a smaller magnitude or later phase of DCP. Between 00
413 and 06 LST, SKIM, CMC, TaiESM1 and ICON produce most of their precipitation (70% – 90%)
414 from the convective parameterization at both sites, while other models produce ~60% of their
415 precipitation at SGP and 40% – 95% of their precipitation at MAO as large-scale precipitation.
416 Although impacted by convective process such as latent heating and detrainment, the large-scale
417 precipitation produced in SCMs is primarily attributed to the prescribed large-scale forcing,
418 which is constrained by the observed surface precipitation. In free-run GCMs, where the large-
419 scale forcing interacts with model physics and is affected by their deficiencies, the simulation of
420 nocturnal precipitation could be even worse (e.g., Tang et al. 2021). Thus, it seems to be
421 necessary to improve the deficiencies in model parameterizations found in the present study. that
422 might potentially contribute to model errors in a less constrained model setup.

423 There is a distinguishing feature that separates these two groups of models: whether or not the
424 model allows elevated convection triggered above the boundary layer. EAMv1, SCAM6 and
425 SMCPCP all use the ZM deep convective scheme with the launching parcel chosen only within

426   the boundary layer. SKIM and TaiESM1 select air parcels below ~700 hPa (σ=0.7) and 600 hPa,
427   respectively, and ICON selects air parcels within 350hPa above the surface. It is natural to
428   hypothesize that allowing convection to occur above the boundary layer is the key to simulate
429   nocturnal convection. In the sensitivity study in Section 4, when the default ZM scheme is
430   modified by unlimiting the launching level, the nocturnal precipitation in EAMv1.trigger is
431   significantly improved compared to default EAMv1. CMC has a separated mid-level convective
432   scheme to capture elevated convection (McTaggart-Cowan et al. 2020). The mid-level scheme
433   exhibits a maximum activity during the night (Figure 10). However, its contribution to the total
434   precipitation is very modest while deep convection contributes the most for nocturnal
435   precipitation. Further sensitivity tests with different thresholds for deep and mid-level convection
436   triggering have shown little sensitivity of the phase of DCP to how active the deep and mid-level
437   schemes are.

438   Figure 11 shows the 00-06 LST mean vertical profiles of Q_1 and Q_2 at SGP and MAO for the
439   nocturnal precipitation events. The observed heating profile is top-heavy at SGP and roughly
440   parabolic at MAO, showing typical convective conditions over mid-latitude continent and
441   tropics, respectively. The condensational drying has a sharper and stronger peak at MAO than
442   SGP. It is interesting to see that all models produce heating and drying peaks at a similar height
443   to that of the observed, despite their wide ranges of convective fraction as shown in Figures 5
444   and 9 (e.g., Schumacher et al. 2004). The reasonable simulation of nocturnal convective heating
445   depth at MAO (Figure 11b) is notable given the poor performance at afternoon convective
446   heating depth (Figure 7b), possibly related to that, afternoon convection is locally-driven while
447   nocturnal convection is propagating organized convection. The magnitude of Q_1 and Q_2 varies
448   among models. SKIM, TaiESM1 and CMC produce similar magnitudes of Q_1 and Q_2
449   comparable with observations, while the other models produce smaller magnitudes (except
450   ICON Q_1 at MAO). The reduction of the Q_1 peak in these models is more prevalent in the upper
451   levels, which may be related to the weaker convective activity that is not sufficient to remove all
452   the instability from the large-scale forcing. The remaining instability in these models is then
453   released at a later time, causing the morning-time precipitation peak seen in Figure 9.

454

4. Sensitivity Study

456   In addition to the default simulations, some modeling centres also performed other simulations
457   using different model versions, physical schemes or configurations. Table 3 shows the
458   information of the simulations included in this section emphasizing their differences from the
459   default models/runs. DCP in SKIM.nudge is very similar to the default runs, so we choose not to
460   show them to make the figures more readable. Moreover, SAM0-UNICON is included in this
461   sensitivity study because of two reasons: firstly, it is developed from SCAM5, with the same
462   turbulence, microphysics and macrophysics schemes but a different convective scheme;

463   secondly, it unifies shallow and deep convection, so we feel it is interesting to compare it with
464   another model with unified shallow and deep convection (EAMv1.SILHS).

465   Figure 12 shows DCP performance of the models for sensitivity study in the afternoon
466   precipitation regime, while Figure 13 shows DCP performance in the nocturnal precipitation
467   regime. EAMv1.trigger uses a modified convective trigger, which uses a dynamic CAPE
468   (dCAPE: CAPE changes due to large-scale advections) to trigger convection and allow air
469   parcels to launch above the boundary layer. The improvement of DCP in GCMs has been
470   demonstrated in Xie et al. (2019), Wang et al. (2020) and (Cui et al. 2021). Here for SCM, the
471   improvement of DCP is also shown at SGP and MAO (Figures 12 and 13) (blue dashed line and
472   open circle). We believe that the dCAPE trigger helps delay the precipitation onset of afternoon
473   precipitation while allowing air parcels to launch above the boundary layer helps convection
474   occur at night.

475   Another independent modification of EAMv1, EAMv1.SILHS, also shows significant
476   improvement on DCP in the two precipitation regimes. Instead of using ZM for deep convection
477   and CLUBB for shallow convection and large-scale clouds and precipitation in the default
478   EAMv1, EAMv1.SILHS uses CLUBB for all shallow convection, deep convection and large-
479   scale clouds and precipitation. Therefore, the convective fraction is zero because it does not
480   separate convective and large-scale precipitation. The CLUBB is interfaced to the microphysics
481   scheme using the subgrid sampler SILHS. It well captures the elevated convection at night as
482   shown in Figure 13, possibly because it does not need a convective trigger nor specification of
483   parcel launching level. For afternoon precipitation, it delays the precipitation onset time on both
484   SGP and MAO (Figure 8), but only produces about half of the observed peak precipitation and
485   ~30% of the harmonic amplitude (Figure 12). This is subject to further improvements.

486   Another model with a unified convective scheme, SAM0-UNICON, is also shown in Figures 12
487   and 13. Note that SAM0-UNICON and SCAM6 both have a tight relationship with SCAM5:
488   SAM0-UNICON has the same turbulence, microphysics and macrophysics schemes as SCAM5,
489   but a different shallow and deep convective scheme. SCAM6 only shares the same deep
490   convective scheme with SCAM5, with turbulence, shallow convection and macrophysics
491   replaced by CLUBB. The DCP performance in SCAM6 is similar as in SCAM5, while SAM0-
492   UNICON shows larger differences with SCAM5. This indicates that DCP is primarily controlled
493   by the deep convective scheme. Since SAM0-UNICON can simulate the complex interactions
494   between subgrid and grid-scale processes such as the transition from shallow to deep convection,
495   it captures well the afternoon precipitation, especially at SGP. However, its performance on
496   nighttime precipitation still needs to be improved. This is consistent with previous work in global
497   simulations (Park 2014b; Tang et al. 2021).

498   Two models conducted sensitivity tests with an interactive land model. SCAM6 is coupled with
499   the community land model version 5.0 (CLM5, Lawrence et al. 2019), while SKIM is coupled
500   with the revised Noah land surface model version 3.4.1 (Koo et al. 2017). SKIM.land performs

501 similar to the default SKIM run, while SCAM6.land performs better than SCAM6, with the early
502 onset of afternoon precipitation (see Figure 8 and Figure 12) and the morning rainfall in
503 nocturnal precipitation days (Figure 13) both reduced. It is interesting to see that SCAM6.land
504 produces much lower latent heat fluxes and higher sensible heat fluxes than observations (Figure
505 14). The estimated ground heat flux is also much larger in SCAM6.land than in other models,
506 with daily mean of 61.7 W/m^2 at SGP and 59.0 W/m^2 at MAO. The corresponding ground heat
507 flux in SCAM6 is $-$ 9.4 W/m^2 at SGP and $-$ 3.9 W/m^2 at MAO, and that in the observations is
508 4.9 W/m^2 at SGP and $-$ 5.3 W/m^2 at MAO. On the other hand, SKIM.land also produces lower
509 latent heat fluxes and higher sensible heat fluxes than observations, likely due to more humid
510 near-surface air or misrepresented surface conditions such as vegetation fraction, land type or
511 soil properties. Its turbulent flux errors are smaller than SCAM6.land, and its ground heat flux is
512 similar with SKIM and observations. Despite the differences in the land models used in
513 SCAM6.land and SKIM.land, it may be inferred that the land-atmospheric interactions in climate
514 models are not well represented so that a model (SCAM6.land) needs to produce more
515 unrealistic surface fluxes in order to get more realistic precipitation in deep convective regimes.

516

5. Summary and Discussions

518 The diurnal cycle of precipitation (DCP) is a problem that GCMs have struggled to represent in
519 past decades (Fiedler et al. 2020). Although the latest GCMs in the recent CMIP6 have shown
520 improvement in simulating DCP (Tang et al. 2021), they still suffer from the persistent problems
521 of too early precipitation and missing nocturnal precipitation.

522 The GEWEX Global Atmospheric System Study (GASS) Panel organized a project focusing on
523 understanding and improving the model capability to simulate diurnal precipitation phenomena
524 through multi-model intercomparison studies against observations. This study focuses on the
525 intercomparison of SCMs to understand what processes control the diurnal cycle of precipitation
526 over different climate regimes and identify the deficiencies and missing physics in current model
527 parameterizations. Instead of focusing on a particular intensive observing period for several days
528 to a few months as in previous SCM intercomparison studies, we have performed long-term
529 hindcast simulations to obtain robust statistics of model performances on DCP. Eleven SCMs
530 from different modeling centers around the world have participated in this project.

531 DCP in twelve summer seasons at a midlatitude land site (SGP) and two continuous years at a
532 tropical land site (MAO) are investigated in this study. The two selected sites have distinguished
533 and representative characteristics of the large-scale environment, clouds and precipitation. The
534 participating SCMs do not always show the same discrepancies at the two sites. This indicates
535 that some parameterization assumptions may not work well across all climate regimes.

536 Two regimes of DCP are examined in this study, one is surface-driven afternoon convection and
537 the other is nocturnal precipitation caused by elevated convection or propagating convective

538 systems. For afternoon convection, precipitation in most SCMs initiated 1 to 4 hours earlier than
539 observation. The early onset of precipitation is more severe at MAO than at SGP. It appears to be
540 associated with two other issues common across all the models for MAO afternoon precipitation
541 cases: a severe deficiency of convective heating in the upper troposphere, and rainfall too evenly
542 spread across times of day. In other words for the MAO afternoon cases, models fail to develop
543 strong deep convection but precipitate too easily from convection in the lower troposphere. At
544 SGP, the early onset of afternoon precipitation may be due to the missing transition of shallow-
545 to-deep convection in climate models. More sophisticated parameterizations that unify shallow
546 and deep convection (e.g., UNICON, CLUBB-SILHS) can improve the early onset problem,
547 although UNICON shows more deficiencies in the precipitation-CRH relationship. For nocturnal
548 precipitation, although all SCMs produce considerable precipitation at night, the partitioning of
549 convective precipitation and large-scale precipitation differ dramatically among models. Models
550 with most of the nocturnal precipitation generated from large-scale are likely driven by the
551 prescribed large-scale forcing. SCMs that produce most of nocturnal precipitation from
552 convection (SKIM, TaiESM1, CMC, ICON and EAMv1.trigger) all allow convection to be
553 triggered above the boundary layer. Although a few recent studies have considered convection
554 moving across grids (Malardel and Bechtold 2019; McTaggart-Cowan et al. 2019b), most SCMs
555 and their parent GCMs still struggle to propagate convection from one grid to another. The
556 capability to detect mid-level instability above the boundary layer is important for them to
557 simulate nocturnal precipitation.

558 Sensitivity studies were performed using continuous nudging runs, different parameterizations,
559 or interactive land models. Using a revised convective trigger specifically targeting improvement
560 on the diurnal cycle of precipitation, EAMv1.trigger shows the importance of dynamically
561 constraining the convective trigger and allowing parcels to launch above the boundary layer in
562 traditional convective parameterizations to produce precipitation at the right time. Another path
563 towards improving DCP is the effort of unifying shallow and deep convection, as seen in SAM0-
564 UNICON and EAMv1.SILHS. On the other hand, in the two land-atmosphere coupled
565 simulations, the one with larger biases in surface turbulent fluxes (SCAM6.land) shows more
566 improvement on DCP. This indicates that the relationship between the land-atmospheric
567 interaction and DCP is complicated and points to the importance of the representation of
568 boundary-layer processes in deep convective regimes. Further study is needed to investigate how
569 the representation of land-atmospheric coupling will influence simulation of DCP.

570 Although not the focus of this study here, the discrepancy in the amplitude of DCP should also
571 be pointed out. In addition to deep and shallow convection, boundary layer processes can highly
572 contribute to the control of the diurnal amplitude (e.g., Koo and Hong 2010). Therefore, a
573 diversity of turbulence schemes (Table 1) might be a source of large spread in diurnal amplitude,
574 which needs to be addressed in future study.

575 This SCM intercomparison study provides insights of which physical processes are essential in
576 climate models to simulate DCP, given a large-scale environment close to the real world. In a

577 global or regional model, the model biases in large-scale dynamic and thermodynamic states and

578 the interactions between the large-scale fields and physics also impact the simulation of DCP.

579 This is not revealed in the SCM study. An intercomparison of global and regional climate models

580 is currently underway and more details will be presented on DCP over broader regions in the

581 near future.

582

596

597 **Appendix: Model schemes and abbreviations in Tables 1, 2 and 3**

598 Bechtold14: convective scheme from Bechtold et al. (2014)

599 CAPE: convective available potential energy

600 CIN: convective inhibition

601 CLUBB: Cloud Layers Unified By Binormals (Golaz et al. 2002; Larson and Golaz 2005; Larson 2017)

602 dCAPE: dynamic CAPE generation rate from large-scale tendency (Xie and Zhang 2000)

603 UW-diag_TKE: University of Washington diagnostic turbulent kinetic energy scheme (Bretherton and
604 Park 2009)

605 GTS: Global Forecast System (GFS) – Taiwan Earth System Model (TaiESM) – Sundqvist scheme (Shiu
606 et al. 2021)

607 HanPan: shallow convection from Han and Pan (2011)

608 HB: turbulent scheme from Holtslag and Boville (1993)

609 Köhler20: cloud cover parameterization from Köhler (2020)

610 KSAS: Korean Integrated Model (KIM, Hong et al. 2018) version of the simplified Arakawa-Schubert
611 deep convection scheme (Han et al. 2020)

612 LCL: lifting condensation level

613 LFC: level of free convection

614 M-Bechtold: modified from Bechtold et al. (2001) (McTaggart-Cowan et al. 2019a)

615 MG: bulk two-moment cloud microphysics (Morrison and Gettelman 2008)

616 MG2: version 2 of MG microphysics (Gettelman et al. 2015)

617 Modified KF: modified from Kain and Fritsch (1990) (McTaggart-Cowan et al. 2019a)

618 Park1: macrophysics from (Park et al. 2014)

619 Park2: macrophysics from (Park et al. 2017)

620 PCH16: macrophysics from (Park et al. 2016)

621 UW-PB09: University of Washington shallow convective scheme (Park and Bretherton 2009)

622 PBL: planetary boundary layer

623 Raschendorfer00: turbulence scheme from Raschendorfer (2000)

624 Seifert08: single moment microphysics from Seifert (2008)

625 Shin-Hong: turbulence scheme from Shin and Hong (2015) with revision of Lee et al. (2018)

626 SILHS: Subgrid Importance Latin Hypercube Sampler (Thayer-Calder et al. 2015; Griffin and Larson
627 2016)

628 Sundqvist: microphysics from Sundqvist et al. (1989)

629 TKE1.5: 1.5 order turbulent kinetic energy scheme from McTaggart-Cowan et al. (2019a)

630 UNICON: Unified convective scheme (Park 2014a, 2014b)

631 Unified stochastic Plume-ZM: Unified Stochastic Mass-flux Cumulus integrated in ZM scheme
632 (Khouider and Leclerc 2019)

633 WSM5: the Weather Research and Forecasting (WRF) single-moment 5-class microphysics scheme
634 (Hong et al. 2004; Bae et al. 2016; Kim and Hong 2018)

635 ZM: Zhang-McFarlane convective scheme (Zhang and McFarlane 1995)

636

637

References:

639 Bae, S. Y., S.-Y. Hong, and K.-S. S. Lim, 2016: Coupling WRF Double-Moment 6-Class Microphysics
640 Schemes to RRTMG Radiation Scheme in Weather Research Forecasting Model. *Advances in*
641 *Meteorology*, **2016,** 5070154**,** 10.1155/2016/5070154.

642 Bašták Ďurán, I., and Coauthors, 2021: The ICON Single-Column Mode. *Atmosphere*, **12,** 906.

643 Bechtold, P., and Coauthors, 2000: A GCSS model intercomparison for a tropical squall line observed
644 during toga-coare. II: Intercomparison of single-column models and a cloud-resolving model. *Quarterly*
645 *Journal of the Royal Meteorological Society*, **126,** 865-888**,** 10.1002/qj.49712656405.

646 Bechtold, P., E. Bazile, F. Guichard, P. Mascart, and E. Richard, 2001: A mass-flux convection scheme
647 for regional and global models. *Quarterly Journal of the Royal Meteorological Society*, **127,** 869-886**,**
648 https://doi.org/10.1002/qj.49712757309.

649 Bechtold, P., J.-P. Chaboureau, A. Beljaars, A. K. Betts, M. Köhler, M. Miller, and J.-L. Redelsperger,
650 2004: The simulation of the diurnal cycle of convective precipitation over land in a global model.
651 *Quarterly Journal of the Royal Meteorological Society*, **130,** 3119-3137**,** 10.1256/qj.03.103.

652 Bechtold, P., and Coauthors, 2008: Advances in simulating atmospheric variability with the ECMWF
653 model: From synoptic to decadal time-scales. *Quarterly Journal of the Royal Meteorological Society*,
654 **134,** 1337-1351**,** https://doi.org/10.1002/qj.289.

655 Bechtold, P., N. Semane, P. Lopez, J.-P. Chaboureau, A. Beljaars, and N. Bormann, 2014: Representing
656 Equilibrium and Nonequilibrium Convection in Large-Scale Models. *Journal of the Atmospheric*
657 *Sciences*, **71,** 734-753**,** 10.1175/jas-d-13-0163.1.

658 Betts, A. K., and C. Jakob, 2002: Study of diurnal cycle of convective precipitation over Amazonia using
659 a single column model. *Journal of Geophysical Research: Atmospheres*, **107,** ACL 25-1-ACL 25-13**,**
660 10.1029/2002jd002264.

661 Bogenschutz, P. A., S. Tang, P. M. Caldwell, S. Xie, W. Lin, and Y. S. Chen, 2020: The E3SM version 1
662 single-column model. *Geosci. Model Dev.*, **13,** 4443-4458**,** 10.5194/gmd-13-4443-2020.

663 Bretherton, C. S., S. K. Krueger, M. C. Wyant, P. Bechtold, E. Van Meijgaard, B. Stevens, and J.
664 Teixeira, 1999: A GCSS Boundary-Layer Cloud Model Intercomparison Study Of The First Astex
665 Lagrangian Experiment. *Boundary-Layer Meteorology*, **93,** 341-380**,** 10.1023/A:1002005429969.

666 Bretherton, C. S., M. E. Peters, and L. E. Back, 2004: Relationships between Water Vapor Path and
667 Precipitation over the Tropical Oceans. *Journal of Climate*, **17,** 1517-1528**,** 10.1175/1520-
668 0442(2004)017<1517:Rbwvpa>2.0.Co;2.

669 Bretherton, C. S., and S. Park, 2009: A New Moist Turbulence Parameterization in the Community
670 Atmosphere Model. *Journal of Climate*, **22,** 3422-3448**,** 10.1175/2008JCLI2556.1.

671 Covey, C., and Coauthors, 2016: Metrics for the Diurnal Cycle of Precipitation: Toward Routine
672 Benchmarks for Climate Models. *Journal of Climate*, **29,** 4461-4471**,** 10.1175/jcli-d-15-0664.1.

673 Cui, Z., G. J. Zhang, Y. Wang, and S. Xie, 2021: Understanding the Roles of Convective Trigger
674 Functions in the Diurnal Cycle of Precipitation in the NCAR CAM5. *Journal of Climate*, **34,** 6473-6489**,**
675 10.1175/jcli-d-20-0699.1.

676 Dai, A., K. E. Trenberth, and T. R. Karl, 1999: Effects of Clouds, Soil Moisture, Precipitation, and Water
677 Vapor on Diurnal Temperature Range. *Journal of Climate*, **12,** 2451-2473**,** 10.1175/1520-
678 0442(1999)012<2451:Eocsmp>2.0.Co;2.

679 Dai, A., 2006: Precipitation Characteristics in Eighteen Coupled Climate Models. *Journal of Climate*, **19,**
680 4605-4630**,** 10.1175/jcli3884.1.

681 Davies, L., and Coauthors, 2013: A single-column model ensemble approach applied to the TWP-ICE
682 experiment. *Journal of Geophysical Research: Atmospheres*, **118,** 6544-6563**,** 10.1002/jgrd.50450.

683 de Rooy, W. C., and Coauthors, 2013: Entrainment and detrainment in cumulus convection: an overview.
684 *Quarterly Journal of the Royal Meteorological Society*, **139,** 1-19**,** 10.1002/qj.1959.

685 Del Genio, A. D., Y. Chen, D. Kim, and M.-S. Yao, 2012: The MJO Transition from Shallow to Deep
686 Convection in CloudSat/CALIPSO Data and GISS GCM Simulations. *Journal of Climate*, **25,** 3755-3770**,**
687 10.1175/jcli-d-11-00384.1.

688 Eyring, V., S. Bony, G. A. Meehl, C. A. Senior, B. Stevens, R. J. Stouffer, and K. E. Taylor, 2016:
689 Overview of the Coupled Model Intercomparison Project Phase 6 (CMIP6) experimental design and
690 organization. *Geosci. Model Dev.*, **9,** 1937-1958**,** 10.5194/gmd-9-1937-2016.

691 Fiedler, S., and Coauthors, 2020: Simulated Tropical Precipitation Assessed across Three Major Phases of
692 the Coupled Model Intercomparison Project (CMIP). *Monthly Weather Review*, **148,** 3653-3680**,**
693 10.1175/mwr-d-19-0404.1.

694 Frenkel, Y., B. Khouider, and A. J. Majda, 2011a: Simple Multicloud Models for the Diurnal Cycle of
695 Tropical Precipitation. Part I: Formulation and the Case of the Tropical Oceans. *Journal of the*
696 *Atmospheric Sciences*, **68,** 2169-2190**,** 10.1175/2011jas3568.1.

697 ——, 2011b: Simple Multicloud Models for the Diurnal Cycle of Tropical Precipitation. Part II: The
698 Continental Regime. *Journal of the Atmospheric Sciences*, **68,** 2192-2207**,** 10.1175/2011jas3600.1.

699 Geerts, B., and Coauthors, 2017: The 2015 Plains Elevated Convection at Night Field Project. *Bulletin of*
700 *the American Meteorological Society*, **98,** 767-786**,** 10.1175/bams-d-15-00257.1.

701 Gettelman, A., H. Morrison, S. Santos, P. Bogenschutz, and P. M. Caldwell, 2015: Advanced Two-
702 Moment Bulk Microphysics for Global Models. Part II: Global Model Solutions and Aerosol–Cloud
703 Interactions. *Journal of Climate*, **28,** 1288-1307**,** 10.1175/jcli-d-14-00103.1.

704 Gettelman, A., J. E. Truesdale, J. T. Bacmeister, P. M. Caldwell, R. B. Neale, P. A. Bogenschutz, and I.
705 R. Simpson, 2019: The Single Column Atmosphere Model Version 6 (SCAM6): Not a Scam but a Tool
706 for Model Evaluation and Development. *Journal of Advances in Modeling Earth Systems*, **11,** 1381-1401**,**
707 10.1029/2018ms001578.

708 Ghan, S., and Coauthors, 2000: A comparison of single column model simulations of summertime
709 midlatitude continental convection. *Journal of Geophysical Research: Atmospheres*, **105,** 2091-2124**,**
710 10.1029/1999JD900971.

711 Golaz, J.-C., V. E. Larson, and W. R. Cotton, 2002: A PDF-Based Model for Boundary Layer Clouds.
712 Part I: Method and Model Description. *Journal of the Atmospheric Sciences*, **59,** 3540-3551**,**
713 10.1175/1520-0469(2002)059<3540:apbmfb>2.0.co;2.

714 Griffin, B. M., and V. E. Larson, 2016: Parameterizing microphysical effects on variances and
715 covariances of moisture and heat content using a multivariate probability density function: a study with
716 CLUBB (tag MVCS). *Geosci. Model Dev.*, **9,** 4273-4295**,** 10.5194/gmd-9-4273-2016.

717 Guichard, F., and Coauthors, 2004: Modelling the diurnal cycle of deep precipitating convection over
718 land with cloud-resolving models and single-column models. *Quarterly Journal of the Royal*
719 *Meteorological Society*, **130,** 3139-3172**,** 10.1256/qj.03.145.

720 Guo, Z., B. M. Griffin, S. Domke, and V. E. Larson, 2021: A parameterization of turbulent dissipation
721 and pressure damping time scales in stably stratified inversions, and its effects on low clouds in global

722   simulations. *Journal of Advances in Modeling Earth Systems*, **n/a,** e2020MS002278,
723   https://doi.org/10.1029/2020MS002278.

724   Han, J.-Y., S.-Y. Hong, and Y. C. Kwon, 2020: The Performance of a Revised Simplified Arakawa–
725   Schubert (SAS) Convection Scheme in the Medium-Range Forecasts of the Korean Integrated Model
726   (KIM). *Weather and Forecasting*, **35,** 1113-1128, 10.1175/waf-d-19-0219.1.

727   Han, J., and H.-L. Pan, 2011: Revision of Convection and Vertical Diffusion Schemes in the NCEP
728   Global Forecast System. *Weather and Forecasting*, **26,** 520-533, 10.1175/waf-d-10-05038.1.

729   Hohenegger, C., and B. Stevens, 2013: Preconditioning Deep Convection with Cumulus Congestus.
730   *Journal of the Atmospheric Sciences*, **70,** 448-464, 10.1175/jas-d-12-089.1.

731   Holloway, C. E., and J. D. Neelin, 2009: Moisture Vertical Structure, Column Water Vapor, and Tropical
732   Deep Convection. *Journal of the Atmospheric Sciences*, **66,** 1665-1683, 10.1175/2008jas2806.1.

733   Holtslag, A. A. M., and B. A. Boville, 1993: Local Versus Nonlocal Boundary-Layer Diffusion in a
734   Global Climate Model. *Journal of Climate*, **6,** 1825-1842, 10.1175/1520-
735   0442(1993)006<1825:Lvnbld>2.0.Co;2.

736   Hong, S.-Y., J. Dudhia, and S.-H. Chen, 2004: A Revised Approach to Ice Microphysical Processes for
737   the Bulk Parameterization of Clouds and Precipitation. *Monthly Weather Review*, **132,** 103-120,
738   10.1175/1520-0493(2004)132<0103:Aratim>2.0.Co;2.

739   Hong, S.-Y., and Coauthors, 2013: The Global/Regional Integrated Model system (GRIMs). *Asia-Pacific*
740   *Journal of Atmospheric Sciences*, **49,** 219-243, 10.1007/s13143-013-0023-0.

741   Hong, S.-Y., and Coauthors, 2018: The Korean Integrated Model (KIM) System for Global Weather
742   Forecasting. *Asia-Pacific Journal of Atmospheric Sciences*, **54,** 267-292, 10.1007/s13143-018-0028-9.

743   Kain, J. S., and J. M. Fritsch, 1990: A One-Dimensional Entraining/Detraining Plume Model and Its
744   Application in Convective Parameterization. *Journal of Atmospheric Sciences*, **47,** 2784-2802,
745   10.1175/1520-0469(1990)047<2784:Aodepm>2.0.Co;2.

746   ——, 1992: The role of the convective "trigger function" in numerical forecasts of mesoscale convective
747   systems. *Meteorl. Atmos. Phys.*, **49,** 93-106, 10.1007/BF01025402.

748   Khairoutdinov, M., and D. Randall, 2006: High-Resolution Simulation of Shallow-to-Deep Convection
749   Transition over Land. *Journal of the Atmospheric Sciences*, **63,** 3421-3436, 10.1175/jas3810.1.

750   Khouider, B., and E. Leclerc, 2019: Toward a Stochastic Relaxation for the Quasi-Equilibrium Theory of
751   Cumulus Parameterization: Multicloud Instability, Multiple Equilibria, and Chaotic Dynamics. *Journal of*
752   *Advances in Modeling Earth Systems*, **11,** 2474-2502.

753   Khouider, B., B. Goswami, R. Phani, and A. Majda, 2021: A shallow-deep unified stochastic mass-flux
754   cumulus parameterization in the single column Community Climate Model. *Journal of Advances in*
755   *Modeling Earth Systems*, Under Review.

756   Kim, S.-Y., and S.-Y. Hong, 2018: The Use of Partial Cloudiness in a Bulk Cloud Microphysics Scheme:
757   Concept and 2D Results. *Journal of the Atmospheric Sciences*, **75,** 2711-2719, 10.1175/jas-d-17-0234.1.

758   Klein, S. A., and Coauthors, 2009: Intercomparison of model simulations of mixed-phase clouds observed
759   during the ARM Mixed-Phase Arctic Cloud Experiment. I: single-layer cloud. *Quarterly Journal of the*
760   *Royal Meteorological Society*, **135,** 979-1002, 10.1002/qj.416.

761   Köhler, M., 2020: Cloud cover. *Chapter 3.8.5 in ICON Tutorial: Working with the ICON Model*, F. Prill,
762   D. Reinert, D. Rieger, and G. Zängl, November 2020, 10.5676/dwd_pub/nwv/icon_tutorial2020.

763

764 Koo, M.-S., and S.-Y. Hong, 2010: Diurnal variations of simulated precipitation over East Asia in two
765 regional climate models. *Journal of Geophysical Research: Atmospheres*, **115,**
766 https://doi.org/10.1029/2009JD012574.

767 Koo, M.-S., S. Baek, K.-H. Seol, and K. Cho, 2017: Advances in land modeling of KIAPS based on the
768 Noah Land Surface Model. *Asia-Pacific Journal of Atmospheric Sciences*, **53,** 361-373**,** 10.1007/s13143-
769 017-0043-2.

770 Kuo, Y.-H., K. A. Schiro, and J. D. Neelin, 2018: Convective Transition Statistics over Tropical Oceans
771 for Climate Model Diagnostics: Observational Baseline. *Journal of the Atmospheric Sciences*, **75,** 1553-
772 1570**,** 10.1175/jas-d-17-0287.1.

773 Kuo, Y.-H., and Coauthors, 2020: Convective Transition Statistics over Tropical Oceans for Climate
774 Model Diagnostics: GCM Evaluation. *Journal of the Atmospheric Sciences*, **77,** 379-403**,** 10.1175/jas-d-
775 19-0132.1.

776 Larson, V. E., and J.-C. Golaz, 2005: Using Probability Density Functions to Derive Consistent Closure
777 Relationships among Higher-Order Moments. *Monthly Weather Review*, **133,** 1023-1042**,**
778 10.1175/mwr2902.1.

779 Larson, V. E., and D. P. Schanen, 2013: The Subgrid Importance Latin Hypercube Sampler (SILHS): a
780 multivariate subcolumn generator. *Geosci. Model Dev.*, **6,** 1813-1829**,** 10.5194/gmd-6-1813-2013.

781 Larson, V. E., 2017: CLUBB-SILHS: A parameterization of subgrid variability in the atmosphere,
782 ArXiv:1711.03675 [Physics].

783 Lawrence, D. M., and Coauthors, 2019: The Community Land Model Version 5: Description of New
784 Features, Benchmarking, and Impact of Forcing Uncertainty. *Journal of Advances in Modeling Earth
785 Systems*, **11,** 4245-4287**,** https://doi.org/10.1029/2018MS001583.

786 Lee, E.-H., E. Lee, R. Park, Y. C. Kwon, and S.-Y. Hong, 2018: Impact of Turbulent Mixing in the
787 Stratocumulus-Topped Boundary Layer on Numerical Weather Prediction. *Asia-Pacific Journal of
788 Atmospheric Sciences*, **54,** 371-384**,** 10.1007/s13143-018-0024-0.

789 Lee, M.-I., S. D. Schubert, M. J. Suarez, J.-K. E. Schemm, H.-L. Pan, J. Han, and S.-H. Yoo, 2008: Role
790 of convection triggers in the simulation of the diurnal cycle of precipitation over the United States Great
791 Plains in a general circulation model. *Journal of Geophysical Research: Atmospheres*, **113,**
792 doi:10.1029/2007JD008984.

793 Lee, W. L., and Coauthors, 2020: Taiwan Earth System Model Version 1: Description and Evaluation of
794 Mean State. *Geosci. Model Dev. Discuss.*, **2020,** 1-43**,** 10.5194/gmd-2019-377.

795 Lenderink, G., and Coauthors, 2004: The diurnal cycle of shallow cumulus clouds over land: A single-
796 column model intercomparison study. *Quarterly Journal of the Royal Meteorological Society*, **130,** 3339-
797 3364**,** 10.1256/qj.03.122.

798 Lin, W., and S. Xie, 2021: Frameworks for Testing and Evaluating Fast Physics Parameterizations in
799 Climate and Weather Forecasting Models. *Fast Physics in Large Scale Atmospheric Models:
800 Parameterization, Evaluation, and Observations*, Y. Liu, P. Kollias, and L. J. Donner, Eds., in publish.

801 Ma, H.-Y., K. Zhang, S. Tang, S. Xie, and R. Fu, 2021a: Evaluation of the Causes of Wet-Season Dry
802 Biases Over Amazonia in CAM5. *Journal of Geophysical Research: Atmospheres*, **126,** e2020JD033859**,**
803 https://doi.org/10.1029/2020JD033859.

804 Ma, H. Y., and Coauthors, 2021b: A multi-year short-range hindcast experiment with CESM1 for
805 evaluating climate model moist processes from diurnal to interannual timescales. *Geosci. Model Dev.*, **14,**
806 73-90**,** 10.5194/gmd-14-73-2021.

807 Malardel, S., and P. Bechtold, 2019: The coupling of deep convection with the resolved flow via the
808 divergence of mass flux in the IFS. *Quarterly Journal of the Royal Meteorological Society*, **145,** 1832-
809 1845**,** https://doi.org/10.1002/qj.3528.

810 Mapes, B., and R. Neale, 2011: Parameterizing Convective Organization to Escape the Entrainment
811 Dilemma. *Journal of Advances in Modeling Earth Systems*, **3,** https://doi.org/10.1029/2011MS000042.

812 Martin, S. T., and Coauthors, 2016: Introduction: Observations and Modeling of the Green Ocean
813 Amazon (GoAmazon2014/5). *Atmos. Chem. Phys.*, **16,** 4785-4797**,** 10.5194/acp-16-4785-2016.

814 McTaggart-Cowan, R., and Coauthors, 2019a: Modernization of Atmospheric Physics Parameterization
815 in Canadian NWP. *Journal of Advances in Modeling Earth Systems*, **n/a,** 10.1029/2019ms001781.

816 McTaggart-Cowan, R., P. A. Vaillancourt, A. Zadra, L. Separovic, S. Corvec, and D. Kirshbaum, 2019b:
817 A Lagrangian Perspective on Parameterizing Deep Convection. *Monthly Weather Review*, **147,** 4127-
818 4149**,** 10.1175/mwr-d-19-0164.1.

819 McTaggart-Cowan, R., P. A. Vaillancourt, L. Separovic, S. Corvec, and A. Zadra, 2020: A Convection
820 Parameterization for Low-CAPE Environments. *Monthly Weather Review*, **148,** 4917-4941**,**
821 10.1175/mwr-d-20-0020.1.

822 Morrison, H., and A. Gettelman, 2008: A New Two-Moment Bulk Stratiform Cloud Microphysics
823 Scheme in the Community Atmosphere Model, Version 3 (CAM3). Part I: Description and Numerical
824 Tests. *Journal of Climate*, **21,** 3642-3659**,** 10.1175/2008JCLI2105.1.

825 Morrison, H., and Coauthors, 2009: Intercomparison of model simulations of mixed-phase clouds
826 observed during the ARM Mixed-Phase Arctic Cloud Experiment. II: Multilayer cloud. *Quarterly*
827 *Journal of the Royal Meteorological Society*, **135,** 1003-1019**,** 10.1002/qj.415.

828 Neale, R. B., and Coauthors, 2012: Description of the NCAR Community Atmosphere Model (CAM 5.0).
829 NCAR Technical Note NCARTN-4861STR, 274 pp.

830 Neelin, J. D., O. Peters, and K. Hales, 2009: The Transition to Strong Convection. *Journal of the*
831 *Atmospheric Sciences*, **66,** 2367-2384**,** 10.1175/2009jas2962.1.

832 Neggers, R. A. J., A. P. Siebesma, and T. Heus, 2012: Continuous Single-Column Model Evaluation at a
833 Permanent Meteorological Supersite. *Bulletin of the American Meteorological Society*, **93,** 1389-1400**,**
834 10.1175/bams-d-11-00162.1.

835 Neggers, R. A. J., and A. P. Siebesma, 2013: Constraining a System of Interacting Parameterizations
836 through Multiple-Parameter Evaluation: Tracing a Compensating Error between Cloud Vertical Structure
837 and Cloud Overlap. *Journal of Climate*, **26,** 6698-6715**,** 10.1175/jcli-d-12-00779.1.

838 Neggers, R. A. J., 2015a: Exploring bin-macrophysics models for moist convective transport and clouds.
839 *Journal of Advances in Modeling Earth Systems*, **7,** 2079-2104**,** 10.1002/2015ms000502.

840 ——, 2015b: Attributing the behavior of low-level clouds in large-scale models to subgrid-scale
841 parameterizations. *Journal of Advances in Modeling Earth Systems*, **7,** 2029-2043**,**
842 https://doi.org/10.1002/2015MS000503.

843 Neggers, R. A. J., and Coauthors, 2017: Single-Column Model Simulations of Subtropical Marine
844 Boundary-Layer Cloud Transitions Under Weakening Inversions. *Journal of Advances in Modeling Earth*
845 *Systems*, **9,** 2385-2412**,** https://doi.org/10.1002/2017MS001064.

846 Oliveira, M. I., and Coauthors, 2020: Planetary boundary layer evolution over the Amazon rainforest in
847 episodes of deep moist convection at the Amazon Tall Tower Observatory. *Atmos. Chem. Phys.*, **20,** 15-
848 27**,** 10.5194/acp-20-15-2020.

849 Park, R.-S., J.-H. Chae, and S.-Y. Hong, 2016: A Revised Prognostic Cloud Fraction Scheme in a Global
850 Forecasting System. *Monthly Weather Review*, **144,** 1219-1229**,** 10.1175/mwr-d-15-0273.1.

851 Park, S., and C. S. Bretherton, 2009: The University of Washington Shallow Convection and Moist
852 Turbulence Schemes and Their Impact on Climate Simulations with the Community Atmosphere Model.
853 *Journal of Climate*, **22,** 3449-3469**,** 10.1175/2008JCLI2557.1.

854 Park, S., 2014a: A Unified Convection Scheme (UNICON). Part I: Formulation. *Journal of the*
855 *Atmospheric Sciences*, **71,** 3902-3930**,** 10.1175/jas-d-13-0233.1.

856 ——, 2014b: A Unified Convection Scheme (UNICON). Part II: Simulation. *Journal of the Atmospheric*
857 *Sciences*, **71,** 3931-3973**,** 10.1175/jas-d-13-0234.1.

858 Park, S., C. S. Bretherton, and P. J. Rasch, 2014: Integrating Cloud Processes in the Community
859 Atmosphere Model, Version 5. *Journal of Climate*, **27,** 6821-6856**,** 10.1175/JCLI-D-14-00087.1.

860 Park, S., E.-H. Baek, B.-M. Kim, and S.-J. Kim, 2017: Impact of detrained cumulus on climate simulated
861 by the Community Atmosphere Model Version 5 with a unified convection scheme. *Journal of Advances*
862 *in Modeling Earth Systems*, **9,** 1399-1411**,** https://doi.org/10.1002/2016MS000877.

863 Park, S., J. Shin, S. Kim, E. Oh, and Y. Kim, 2019: Global Climate Simulated by the Seoul National
864 University Atmosphere Model Version 0 with a Unified Convection Scheme (SAM0-UNICON). *Journal*
865 *of Climate*, **32,** 2917-2949**,** 10.1175/jcli-d-18-0796.1.

866 Petch, J., and Coauthors, 2014: Evaluation of intercomparisons of four different types of model
867 simulating TWP-ICE. *Quarterly Journal of the Royal Meteorological Society*, **140,** 826-837**,**
868 10.1002/qj.2192.

869 Pithan, F., and Coauthors, 2016: Select strengths and biases of models in representing the Arctic winter
870 boundary layer over sea ice: the Larcform 1 single column model intercomparison. *Journal of Advances*
871 *in Modeling Earth Systems*, **8,** 1345-1357**,** https://doi.org/10.1002/2016MS000630.

872 Randall, D. A., K.-M. Xu, R. J. C. Somerville, and S. Iacobellis, 1996: Single-Column Models and Cloud
873 Ensemble Models as Links between Observations and Climate Models. *Journal of Climate*, **9,** 1683-1697**,**
874 10.1175/1520-0442(1996)009<1683:SCMACE>2.0.CO;2.

875 Rasch, P. J., and Coauthors, 2019: An Overview of the Atmospheric Component of the Energy Exascale
876 Earth System Model. *Journal of Advances in Modeling Earth Systems*, **11,** 2377-2411**,**
877 10.1029/2019ms001629.

878 Raschendorfer, M., 2000: The New Turbulence Parameterization in the Lokal-Modell of DWD. *Research*
879 *Activities in Atmospheric and Oceanic Modelling*, WMO/TD-No.987, pg 4.30-4.31.

880 Rio, C., F. Hourdin, J. Y. Grandpeix, and J. P. Lafore, 2009: Shifting the diurnal cycle of parameterized
881 deep convection over land. *Geophysical Research Letters*, **36,** 10.1029/2008GL036779.

882 Ruppert, J. H., and R. H. Johnson, 2015: Diurnally Modulated Cumulus Moistening in the Preonset Stage
883 of the Madden–Julian Oscillation during DYNAMO. *Journal of the Atmospheric Sciences*, **72,** 1622-
884 1647**,** 10.1175/JAS-D-14-0218.1.

885 Rutledge, S. A., and P. V. Hobbs, 1984: The Mesoscale and Microscale Structure and Organization of
886 Clouds and Precipitation in Midlatitude Cyclones. XII: A Diagnostic Modeling Study of Precipitation
887 Development in Narrow Cold-Frontal Rainbands. *Journal of Atmospheric Sciences*, **41,** 2949-2972**,**
888 10.1175/1520-0469(1984)041<2949:Tmamsa>2.0.Co;2.

889 Schumacher, C., R. A. Houze, and I. Kraucunas, 2004: The Tropical Dynamical Response to Latent
890 Heating Estimates Derived from the TRMM Precipitation Radar. *Journal of the Atmospheric Sciences*,
891 **61,** 1341-1358**,** 10.1175/1520-0469(2004)061<1341:TTDRTL>2.0.CO;2.

892   Seifert, A., 2008: A Revised Cloud Microphysical Parameterization for COSMO-LME. *COSMO Newsl*,
893   **7,** 25-28**,** http://www.cosmo-
894   model.org/content/model/documentation/newsLetters/newsLetter07/cnl7_seifert.pdf.

895   Shin, H. H., and S.-Y. Hong, 2015: Representation of the Subgrid-Scale Turbulent Transport in
896   Convective Boundary Layers at Gray-Zone Resolutions. *Monthly Weather Review*, **143,** 250-271**,**
897   10.1175/mwr-d-14-00116.1.

898   Shiu, C. J., and Coauthors, 2021: GTS v1.0: a macrophysics scheme for climate models based on a
899   probability density function. *Geosci. Model Dev.*, **14,** 177-204**,** 10.5194/gmd-14-177-2021.

900   Stephens, G. L., and Coauthors, 2010: Dreary state of precipitation in global models. *Journal of*
901   *Geophysical Research: Atmospheres*, **115,** https://doi.org/10.1029/2010JD014532.

902   Stratton, R. A., and A. J. Stirling, 2012: Improving the diurnal cycle of convection in GCMs. *Quarterly*
903   *Journal of the Royal Meteorological Society*, **138,** 1121-1134**,** 10.1002/qj.991.

904   Sun, Y., S. Solomon, A. Dai, and R. W. Portmann, 2007: How Often Will It Rain? *Journal of Climate*,
905   **20,** 4801-4818**,** 10.1175/jcli4263.1.

906   Sundqvist, H., E. Berge, and J. E. Kristjánsson, 1989: Condensation and Cloud Parameterization Studies
907   with a Mesoscale Numerical Weather Prediction Model. *Monthly Weather Review*, **117,** 1641-1657**,**
908   10.1175/1520-0493(1989)117<1641:Cacpsw>2.0.Co;2.

909   Tang, S., and Coauthors, 2016: Large-scale vertical velocity, diabatic heating and drying profiles
910   associated with seasonal and diurnal variations of convective systems observed in the GoAmazon2014/5
911   experiment. *Atmos. Chem. Phys.*, **16,** 14249-14264**,** 10.5194/acp-16-14249-2016.

912   Tang, S., and Coauthors, 2019: Differences in Eddy-Correlation and Energy-Balance Surface Turbulent
913   Heat Flux Measurements and Their Impacts on the Large-Scale Forcing Fields at the ARM SGP Site.
914   *Journal of Geophysical Research: Atmospheres*, **124,** 3301-3318**,** 10.1029/2018jd029689.

915   Tang, S., P. Gleckler, S. Xie, J. Lee, M.-S. Ahn, C. Covey, and C. Zhang, 2021: Evaluating the Diurnal
916   and Semidiurnal Cycle of Precipitation in CMIP6 Models Using Satellite- and Ground-Based
917   Observations. *Journal of Climate*, **34,** 3189-3210**,** 10.1175/jcli-d-20-0639.1.

918   Taylor, K. E., R. J. Stouffer, and G. A. Meehl, 2012: An Overview of CMIP5 and the Experiment Design.
919   *Bulletin of the American Meteorological Society*, **93,** 485-498**,** 10.1175/bams-d-11-00094.1.

920   Thayer-Calder, K., and Coauthors, 2015: A unified parameterization of clouds and turbulence using
921   CLUBB and subcolumns in the Community Atmosphere Model. *Geosci. Model Dev.*, **8,** 3801-3821**,**
922   10.5194/gmd-8-3801-2015.

923   Tian, Y., Y. Zhang, S. A. Klein, and C. Schumacher, 2021: Interpreting the Diurnal Cycle of Clouds and
924   Precipitation in the ARM GoAmazon Observations: Shallow to Deep Convection Transition. *Journal of*
925   *Geophysical Research: Atmospheres*, **126,** e2020JD033766**,** https://doi.org/10.1029/2020JD033766.

926   Trenberth, K. E., A. Dai, R. M. Rasmussen, and D. B. Parsons, 2003: The Changing Character of
927   Precipitation. *Bulletin of the American Meteorological Society*, **84,** 1205-1218**,** 10.1175/bams-84-9-1205.

928   Varble, A. C., and Coauthors, 2021: Utilizing a Storm-Generating Hotspot to Study Convective Cloud
929   Transitions: The CACTI Experiment. *Bulletin of the American Meteorological Society*, **102,** E1597-
930   E1620**,** 10.1175/bams-d-20-0030.1.

931   Wang, Y.-C., and H.-H. Hsu, 2019: Improving diurnal rainfall phase over the Southern Great Plains in
932   warm seasons by using a convective triggering design. *International Journal of Climatology*, **39,** 5181-
933   5190**,** 10.1002/joc.6117.

934   Wang, Y.-C., S. Xie, S. Tang, and W. Lin, 2020: Evaluation of an Improved Convective Triggering
935   Function: Observational Evidence and SCM Tests. *Journal of Geophysical Research: Atmospheres*, **125,**
936   e2019JD031651**,** 10.1029/2019jd031651.

937   Wang, Y., L. Zhou, and K. Hamilton, 2007: Effect of Convective Entrainment/Detrainment on the
938   Simulation of the Tropical Precipitation Diurnal Cycle. *Monthly Weather Review*, **135,** 567-585**,**
939   10.1175/mwr3308.1.

940   Wang, Y. C., H. L. Pan, and H. H. Hsu, 2015: Impacts of the triggering function of cumulus
941   parameterization on warm‐season diurnal rainfall cycles at the Atmospheric Radiation Measurement
942   Southern Great Plains site. *Journal of Geophysical Research: Atmospheres*, **120,** 10,681-10,702**,**
943   doi:10.1002/2015JD023337.

944   Wei, Y., Z. Pu, and C. Zhang, 2020: Diurnal Cycle of Precipitation Over the Maritime Continent Under
945   Modulation of MJO: Perspectives From Cloud-Permitting Scale Simulations. *Journal of Geophysical*
946   *Research: Atmospheres*, **125,** e2020JD032529**,** https://doi.org/10.1029/2020JD032529.

947   Wyant, M. C., and Coauthors, 2007: A single-column model intercomparison of a heavily drizzling
948   stratocumulus-topped boundary layer. *Journal of Geophysical Research: Atmospheres*, **112,**
949   10.1029/2007jd008536.

950   Xie, S., and M. Zhang, 2000: Impact of the convection triggering function on single‐column model
951   simulations. *Journal of Geophysical Research: Atmospheres*, **105,** 14983-14996**,**
952   doi:10.1029/2000JD900170.

953   Xie, S., and Coauthors, 2002: Intercomparison and evaluation of cumulus parametrizations under
954   summertime midlatitude continental conditions. *Quarterly Journal of the Royal Meteorological Society*,
955   **128,** 1095-1135**,** 10.1256/003590002320373229.

956   Xie, S., R. T. Cederwall, and M. Zhang, 2004: Developing long-term single-column model/cloud system–
957   resolving model forcing data using numerical weather prediction products constrained by surface and top
958   of the atmosphere observations. *Journal of Geophysical Research*, **109,** 10.1029/2003jd004045.

959   Xie, S., and Coauthors, 2005: Simulations of midlatitude frontal clouds by single-column and cloud-
960   resolving models during the Atmospheric Radiation Measurement March 2000 cloud intensive
961   operational period. *Journal of Geophysical Research: Atmospheres*, **110,** D15S03**,**
962   10.1029/2004JD005119.

963   Xie, S., and Coauthors, 2018: Understanding Cloud and Convective Characteristics in Version 1 of the
964   E3SM Atmosphere Model. *Journal of Advances in Modeling Earth Systems*, **10,** 2618-2644**,**
965   doi:10.1029/2018MS001350.

966   Xie, S., and Coauthors, 2019: Improved Diurnal Cycle of Precipitation in E3SM With a Revised
967   Convective Triggering Function. *Journal of Advances in Modeling Earth Systems*, **11,** 2290-2310**,**
968   10.1029/2019ms001702.

969   Xu, K.-M., and Coauthors, 2005: Modeling springtime shallow frontal clouds with cloud-resolving and
970   single-column models. *Journal of Geophysical Research: Atmospheres*, **110,** 10.1029/2004JD005153.

971   Yanai, M., S. Esbensen, and J.-H. Chu, 1973: Determination of Bulk Properties of Tropical Cloud
972   Clusters from Large-Scale Heat and Moisture Budgets. *Journal of the Atmospheric Sciences*, **30,** 611-627**,**
973   10.1175/1520-0469(1973)030<0611:DOBPOT>2.0.CO;2.

974   Zängl, G., D. Reinert, P. Rípodas, and M. Baldauf, 2015: The ICON (ICOsahedral Non-hydrostatic)
975   modelling framework of DWD and MPI-M: Description of the non-hydrostatic dynamical core. *Quarterly*
976   *Journal of the Royal Meteorological Society*, **141,** 563-579**,** https://doi.org/10.1002/qj.2378.

977 Zermeño-Díaz, D. M., C. Zhang, P. Kollias, and H. Kalesse, 2015: The Role of Shallow Cloud
978 Moistening in MJO and Non-MJO Convective Events over the ARM Manus Site. *Journal of the*
979 *Atmospheric Sciences*, **72,** 4797-4820**,** 10.1175/JAS-D-14-0322.1.

980 Zhang, G. J., and N. A. McFarlane, 1995: Sensitivity of climate simulations to the parameterization of
981 cumulus convection in the Canadian climate centre general circulation model. *Atmosphere-Ocean*, **33,**
982 407-446**,** 10.1080/07055900.1995.9649539.

983 Zhang, G. J., 2003: Roles of tropospheric and boundary layer forcing in the diurnal cycle of convection in
984 the U.S. southern great plains. *Geophysical Research Letters*, **30,** doi:10.1029/2003GL018554.

985 Zhang, M., and J. Lin, 1997: Constrained Variational Analysis of Sounding Data Based on Column-
986 Integrated Budgets of Mass, Heat, Moisture, and Momentum: Approach and Application to ARM
987 Measurements. *Journal of the Atmospheric Sciences*, **54,** 1503-1524**,** 10.1175/1520-
988 0469(1997)054<1503:CVAOSD>2.0.CO;2.

989 Zhang, M., J. Lin, R. T. Cederwall, J. J. Yio, and S. C. Xie, 2001: Objective Analysis of ARM IOP Data:
990 Method and Sensitivity. *Monthly Weather Review*, **129,** 295-311**,** 10.1175/1520-
991 0493(2001)129<0295:OAOAID>2.0.CO;2.

992 Zhang, M., R. C. J. Somerville, and S. Xie, 2016: The SCM Concept and Creation of ARM Forcing
993 Datasets. *Meteorological Monographs*, **57,** 24.1-24.12**,** doi:10.1175/AMSMONOGRAPHS-D-15-0040.1.

994 Zhang, Y., and S. A. Klein, 2010: Mechanisms Affecting the Transition from Shallow to Deep
995 Convection over Land: Inferences from Observations of the Diurnal Cycle Collected at the ARM
996 Southern Great Plains Site. *Journal of the Atmospheric Sciences*, **67,** 2943-2959**,**
997 10.1175/2010JAS3366.1.

998 Zhu, P., and Coauthors, 2005: Intercomparison and Interpretation of Single-Column Model Simulations
999 of a Nocturnal Stratocumulus-Topped Marine Boundary Layer. *Monthly Weather Review*, **133,** 2741-
1000 2758**,** 10.1175/mwr2997.1.

1001

1002   Table Captions:

1003   Table 1: Participating models and their basic information

1004   Table 2: Deep convective parameterizations in the participating SCMs

1005   Table 3: Model information for sensitivity study.

1006

1007   Figure Captions:

1008   Figure 1: (Top) the composite diurnal cycle timeseries and (bottom) the harmonic dial plots of
1009   total precipitation averaged for the long-term simulation periods at (left) SGP and (right) MAO.
1010   The gray shading in the timeseries indicates 1.96× standard error (95% confidence) of the
1011   observed precipitation. The radius and phase of the harmonic dial plots represent the amplitude
1012   (mm/day) and the peak hour (LST), respectively, of the first Fourier component of DCP.

1013   Figure 2: As in Figure 1 but for (left) wet season (December – March) and (right) dry season
1014   (July – October) at MAO.

1015   Figure 3: Diurnal cycle of cloud fraction from observations and simulations at (left) SGP and
1016   (right) MAO.

1017   Figure 4: The relationship between precipitation and CRH for (left) SGP and (right) MAO: (top)
1018   the precipitation amount averaged for each CRH bin; (middle) the probability of precipitation
1019   exceeding 1 mm/day for each CRH bin; (bottom) the occurrence frequency of each CRH bin.
1020   CRH is binned in intervals of 2%.

1021   Figure 5: Diurnal cycle timeseries of (top) total precipitation rate, (middle) convective
1022   precipitation fraction, and (bottom) harmonic dial plots of total precipitation averaged for the
1023   selected afternoon precipitation days during the long-term simulation periods at (left) SGP and
1024   (right) MAO.

1025   Figure 6: Percentage of days that the diurnal maximum precipitation occurs at each hour. The
1026   total number of cases are 136 days for SGP and 111 days for MAO.

1027   Figure 7: (Top) apparent heating (Q_1) and (bottom) drying (Q_2) averaged between 12 and 20 LST
1028   for selected afternoon precipitation days during the long-term simulation periods at (left) SGP
1029   and (right) MAO.

1030   Figure 8: The mean (dot, circle or diamond), median (cross), 25th and 75th percentiles (vertical
1031   lines) of precipitation onset time for the afternoon precipitation days at (left) SGP and (right)
1032   MAO. Models for sensitivity studies in Section 4 are also shown here in thin lines.

1033   Figure 9: As in Figure 5 but for selected nocturnal precipitation days.

1034 Figure 10: Precipitation rates from different components in CMC model for selected nocturnal
1035 precipitation days.

1036 Figure 11: Q_1 and Q_2 averaged between 00 and 06 LST for selected nocturnal precipitation days
1037 at (left) SGP and (right) MAO.

1038 Figure 12: As in Figure 5 but for selected models/configurations for sensitivity study. Sensitivity
1039 runs are indicated by dashed/dotted lines and open symbols. Note that the convective
1040 precipitation fraction for EAMv1.SILHS (blue dotted line) is zero because the convective and
1041 large-scale precipitation is unified in CLUBB-SILHS.

1042 Figure 13: As in Figure 12 but for nocturnal precipitation days.

1043 Figure 14: The diurnal cycle of (top) surface latent heat, (middle) sensible heat fluxes and
1044 (bottom) ground heat flux (net radiative fluxes minus latent and sensible heat fluxes) averaged
1045 for the long-term simulation periods at (left) SGP and (right) MAO. The diurnal cycle averaged
1046 in afternoon and nocturnal precipitation days have similar performance (not shown).

1047

Table 1: Participating models and their basic information

Model name	Full name	Vertical levels	Timestep	turbulence	Stratiform clouds	Shallow convection	References	Contact Person
EAMv1	The E3SM* Atmospheric Model V1	72	30min	CLUBB	MG2, CLUBB	CLUBB	Rasch et al. (2019); Bogenschutz et al. (2020)	Shaocheng Xie, Shuaiqi Tang
EAMv1.trigger**	EAMv1 with revised convective trigger	72	30min	CLUBB	MG2, CLUBB	CLUBB	Xie et al. (2019)	Shaocheng Xie, Shuaiqi Tang
EAMv1.SILHS	EAMv1 with CLUBB-SILHS	72	30min	CLUBB	MG2, CLUBB-SILHS	CLUBB-SILHS	Guo et al. (2021)	Vincent Larson, Zhun Guo
SCAM6	Single Column Atmosphere Model Version 6	32	20min	CLUBB	MG2, CLUBB	CLUBB	Gettelman et al. (2019)	Shuaiqi Tang
SCAM5	Single Column Atmosphere Model Version 5	30	20min	UW-diag_TKE	MG, Park1	UW-PB09	Neale et al. (2012)	Shuaiqi Tang
SAM0-UNICON	Seoul National University Atmosphere Model	30	20min	UW-diag_TKE	MG, Park2	UNICON	Park et al. (2019)	Sungsu Park, Jihoon Shin
SKIM	Single Column Korean Integrated Model	64	10min	Shin-Hong	WSM5, PCH16	HanPan	Hong et al. (2013); Hong et al. (2018)	Myung-Seo Koo, Song-You Hong
CMC	Canadian Meteorological Center	84	450sec	TKE1.5	Sundqvist	M-Bechtold	McTaggart-Cowan et al. (2019a)	Paul Vaillancourt, Jing Yang
SMCPCP	Stochastic MultiCloud Plume Convective Parameterization	30	20min	HB	MG, Park1	Unified Stochastic Plume-ZM	Khouider et al. (2021)	Boualem Khouider, Phani Murali Krishna
TaiESM1	Taiwan Earth System Model Version 1	30	30min	UW-diag_TKE	MG, GTS	UW-PB09	Lee et al. (2020)	Yi-Chi Wang
ICON	Icosahedral Nonhydrostatic Weather and Climate Model	90	2min	Raschendorfer00	Seifert08, Köhler20	Bechtold14	Zängl et al. (2015); Bašták Ďurán et al. (2021)	Martin Köhler, Daniel Klocke

*the full names and references of the acronyms and physical schemes are given in the Appendix.

**The results of EAMv1.trigger, EAMv1.SILHS and SCAM5 are only shown in the sensitivity studies in Section 4.

Table 2: Deep convective parameterizations in the participating SCMs

Model name	Deep convection	closure	Convective trigger	downdraft	reference
EAMv1	Zhang-McFarlane scheme (ZM)	Dilute CAPE	(1) CAPE >70 J/kg (2) The air parcel launch level is chosen within the boundary layer	Starts from updraft-top mass flux	Xie et al. (2018)
EAMv1.trigger	ZM with revised convective trigger	Dilute CAPE	(1) CAPE >0 (2) dCAPE >0 (3) The air parcel launch level is chosen between the surface and 600 hPa	Same as EAMv1	Xie et al. (2019)
EAMv1.SILHS	CLUBB-SILHS	No explicit closure	Not needed	Rain evaporation affect fluxes	Thayer-Calder et al. (2015); Griffin and Larson (2016)
SCAM6	ZM	Dilute CAPE	(1) CAPE >70 J/kg (2) The air parcel launch level is chosen within the boundary layer	Downdraft starts from updraft-top mass flux	Gettelman et al. (2019)
SCAM5	ZM	Dilute CAPE	Same as SCAM6	Same as SCAM6	Neale et al. (2012)
SAM0-UNICON	UNICON	No explicit closure	Not needed	Downdraft generated from updraft	Park (2014a, 2014b)
SKIM	KSAS	Quasi-equilibrium closure considering boundary-layer forcing	(1) $P_{parcel\_start} - P_{LFC} < P_{crit}(RH_{low})$ (2) $P_{LFC\_w/o\_ent} - P_{LFC\_w/\_ent} < 25$ hPa (3) $CIN < -120$ m^2 s^{-2} (4) cloud depth > 150 hPa (5) cloud work function > 0	Starts from the level of minimum moist static energy between LFC and 450 hPa	Han et al. (2020)
CMC	Modified Kain-Fritsch (KF) with a mid-level elevated convective scheme	CAPE	(1) mixed parcel from PBL lifted to LCL to which a temperature perturbation is added is buoyant (2) cloud depth > 3000 m	Initiated at level of free sink	Kain and Fritsch (1990, 1992); McTaggart-Cowan et al. (2020)
SMCPCP	Unified Stochastic Plume-ZM	Weighted kinetic energy and CAPE	Same as SCAM6	Same as SCAM6	Khouider et al. (2021)
TaiESM1	ZM with revised convective trigger	Dilute CAPE	(1) CAPE >70 J/kg (2) $P_{parcel\_start} - P_{LFC} < 150$hPa (3) The air parcel launch level is chosen between the surface and 600 hPa	Same as SCAM6	Wang and Hsu (2019)
ICON	Bechtold14	CAPE	Entraining parcels starting with levels up to 350hPa above the surface that must detect cloud layer thinker than 200hPa.	Starts from Level of Free Sinking (LFS) $M(LFS) = -0.3M$ (up,base)	Bechtold et al. (2014)

Table 3: Model information for sensitivity study.

Model name	Model features	Reference
EAMv1	Deep convection: ZM with convective trigger: (1) CAPE >70 J/kg (2) The air parcel launch level is chosen within the boundary layer	
EAMv1.trigger	Deep convection: ZM with convective trigger: (1) CAPE >0 (2) dCAPE >0 (3) The air parcel launch level is chosen between the surface and 600 hPa	Xie et al. (2019)
EAMv1.SILHS	Deep convection: CLUBB-SILHS	Thayer-Calder et al. (2015); Larson (2017)
SAM0-UNICON	Turbulence: diag_TKE Stratiform clouds: MG, Park1 Shallow Convection: UNICON Deep convection: UNICON	Park et al. (2019)
SCAM6	Turbulence: CLUBB Stratiform clouds: MG2, CLUBB Shallow Convection: CLUBB Deep convection: ZM	Gettelman et al. (2019)
SCAM5	Turbulence: diag_TKE Stratiform clouds: MG, Park1 Shallow Convection: PB09 Deep convection: ZM	Neal et al. (2012)
SCAM6.land	Interactive land	
SKIM.land	Interactive land	
SKIM.nudge	Nudging temperature and moisture	
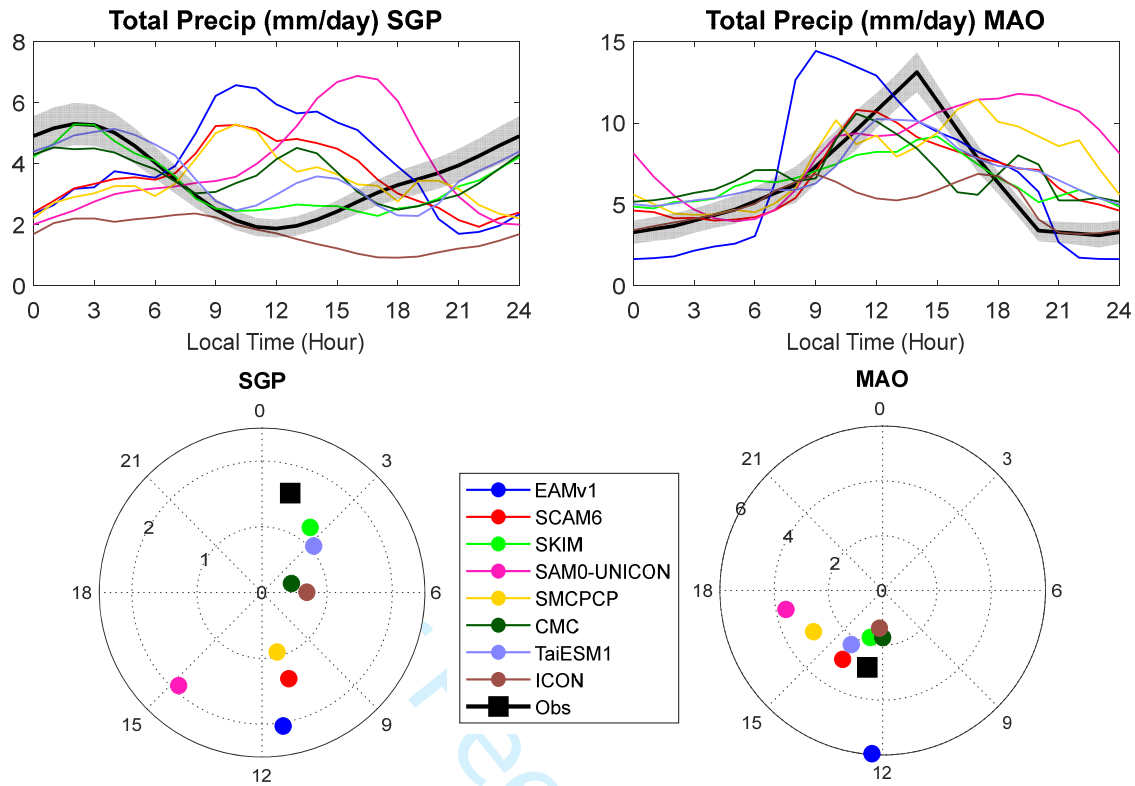
Figure 1: (Top) the composite diurnal cycle timeseries and (bottom) the harmonic dial plots of total precipitation averaged for the long-term simulation periods at (left) SGP and (right) MAO. The gray shading in the timeseries indicates 1.96× standard error (95% confidence) of the observed precipitation. The radius and phase of the harmonic dial plots represent the amplitude (mm/day) and the peak hour (LST), respectively, of the first Fourier component of DCP.
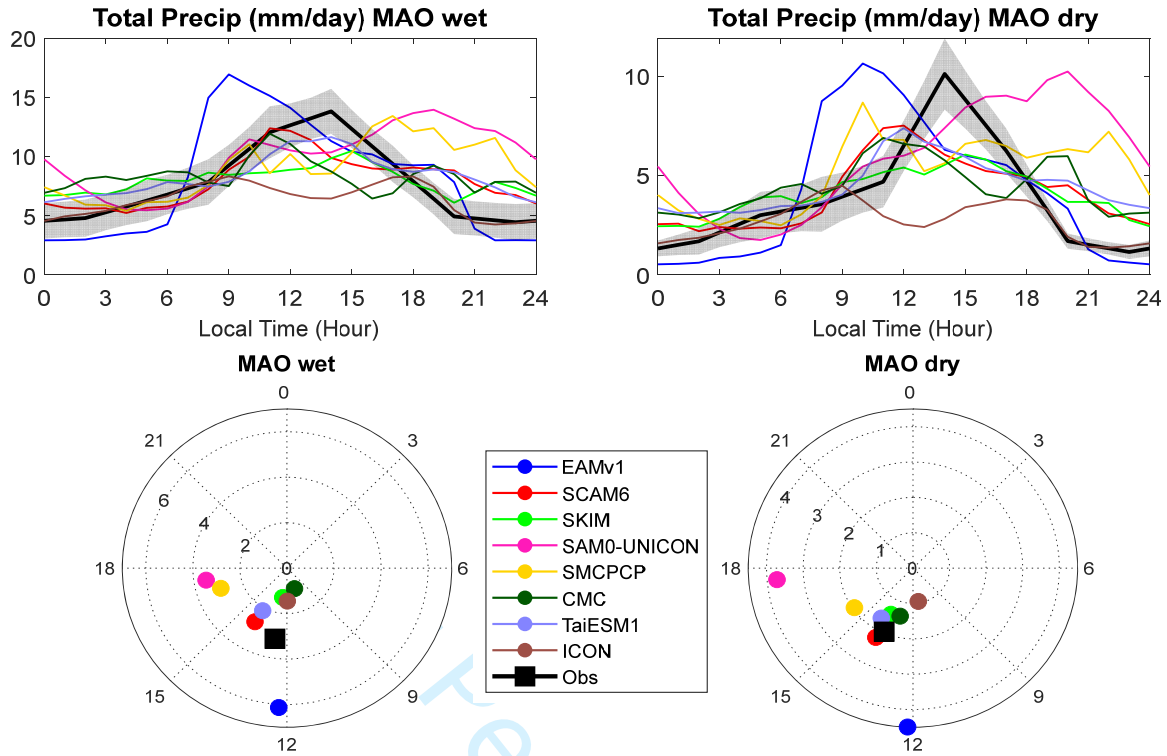
Figure 2: As in Figure 1 but for (left) wet season (December – March) and (right) dry season (July – October) at MAO.
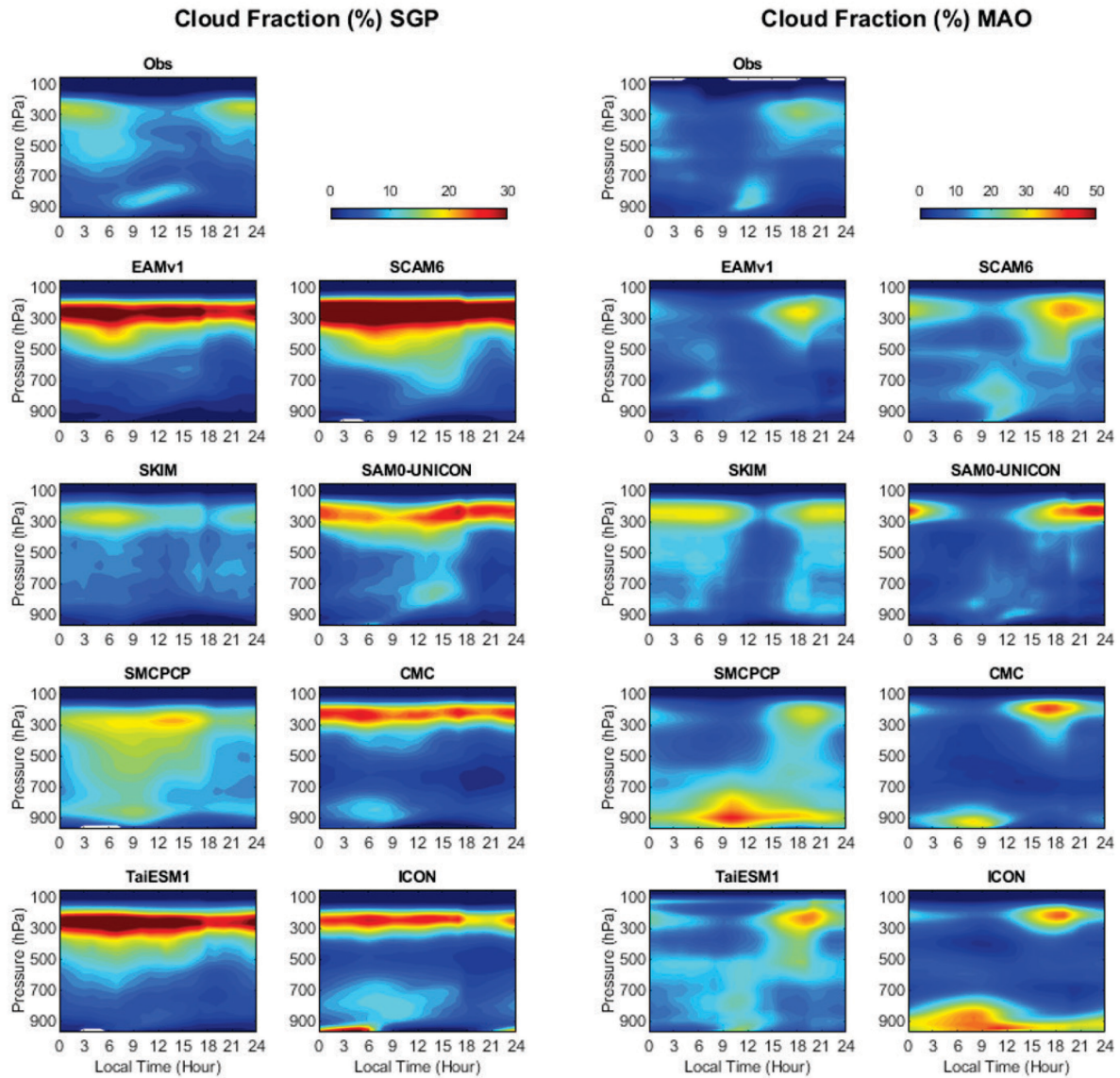
Figure 3: Diurnal cycle of cloud fraction from observations and simulations at (left) SGP and (right) MAO.
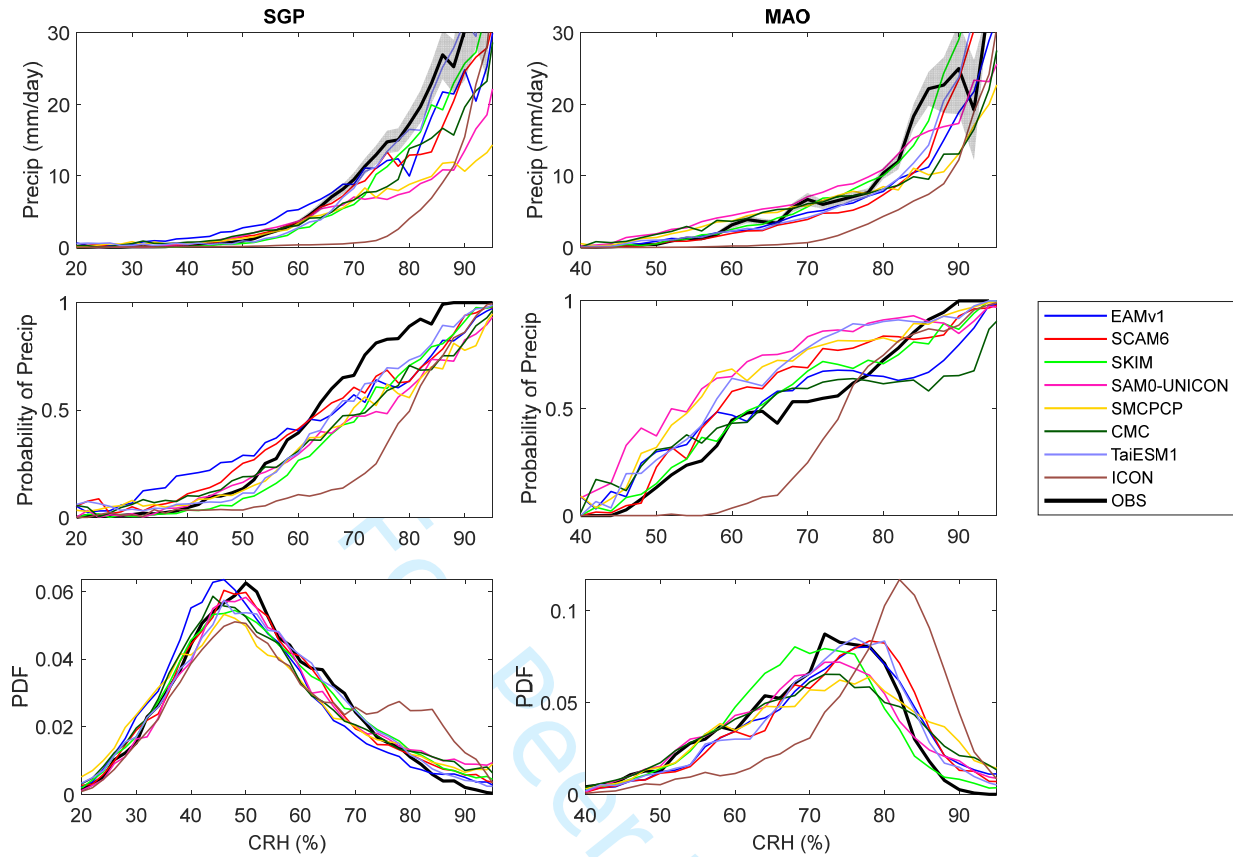
Figure 4: The relationship between precipitation and CRH for (left) SGP and (right) MAO: (top) the precipitation amount averaged for each CRH bin; (middle) the probability of precipitation exceeding 1 mm/day for each CRH bin; (bottom) the occurrence frequency of each CRH bin. CRH is binned in intervals of 2%.
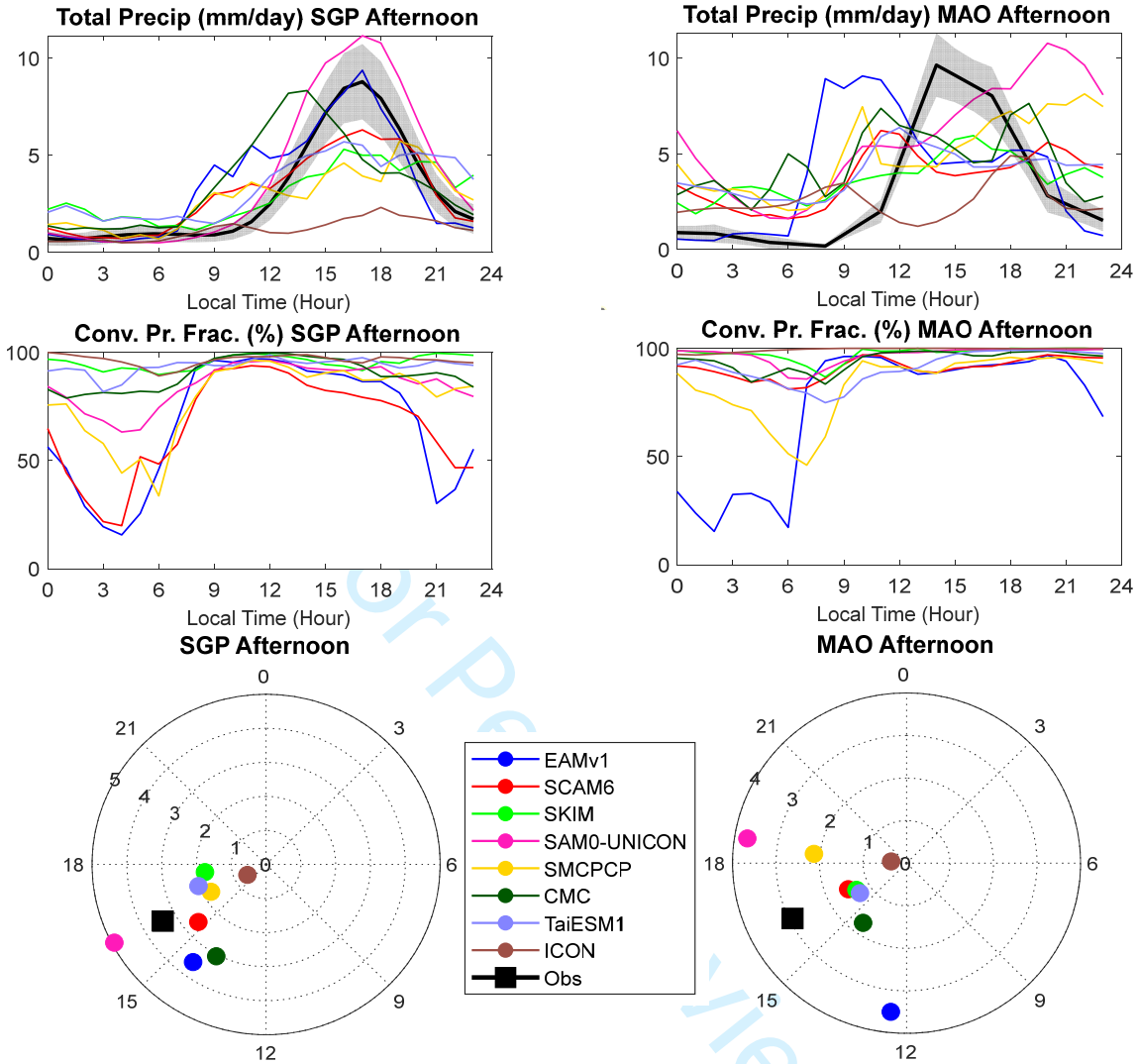
Figure 5: Diurnal cycle timeseries of (top) total precipitation rate, (middle) convective precipitation fraction, and (bottom) harmonic dial plots of total precipitation averaged for the selected afternoon precipitation days during the long-term simulation periods at (left) SGP and (right) MAO.
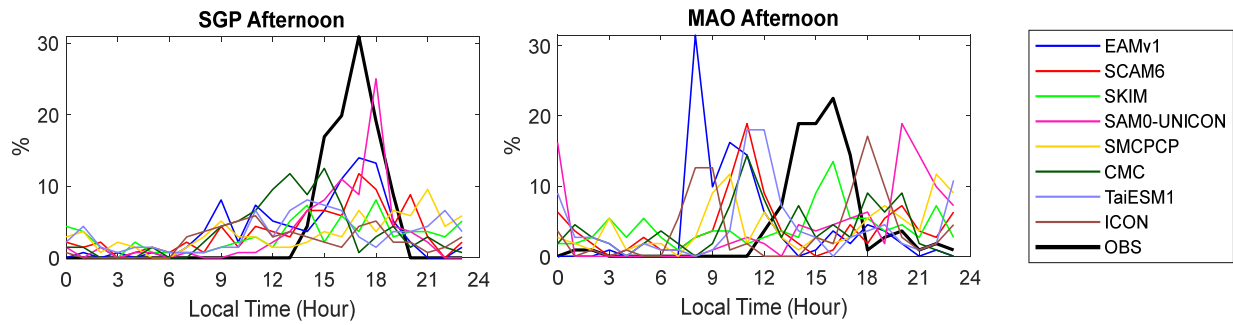
Figure 6: Percentage of days that the diurnal maximum precipitation occurs at each hour. The total number of cases are 136 days for SGP and 111 days for MAO.
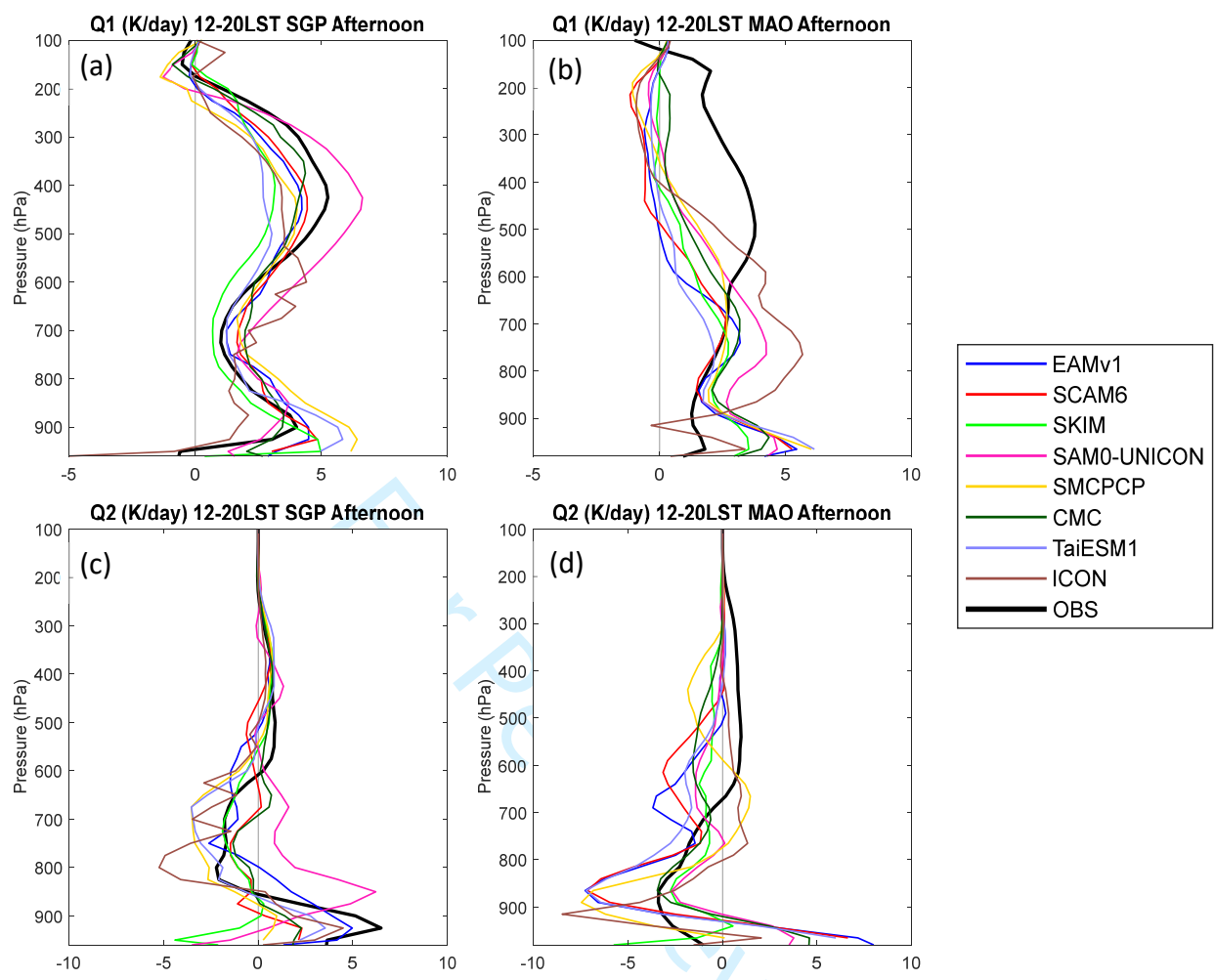
Figure 7: (Top) apparent heating (Q_1) and (bottom) drying (Q_2) averaged between 12 and 20 LST for selected afternoon precipitation days during the long-term simulation periods at (left) SGP and (right) MAO.
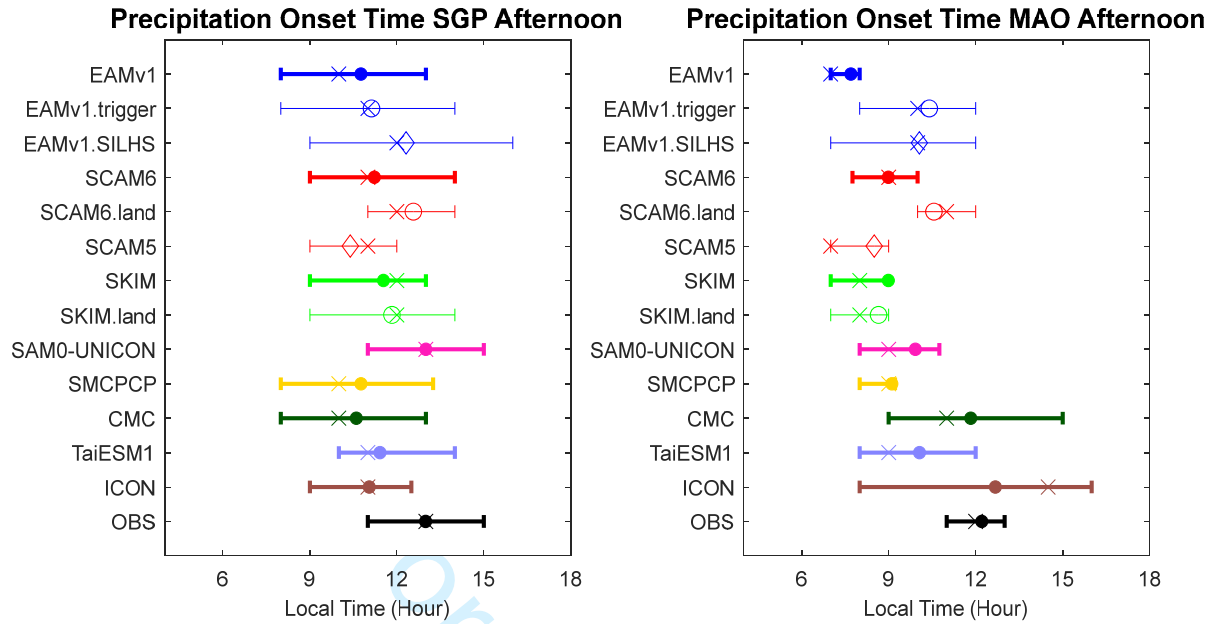
Figure 8: The mean (dot, circle or diamond), median (cross), 25th and 75th percentiles (vertical lines) of precipitation onset time for the afternoon precipitation days at (left) SGP and (right) MAO. Models for sensitivity studies in Section 4 are also shown here in thin lines.
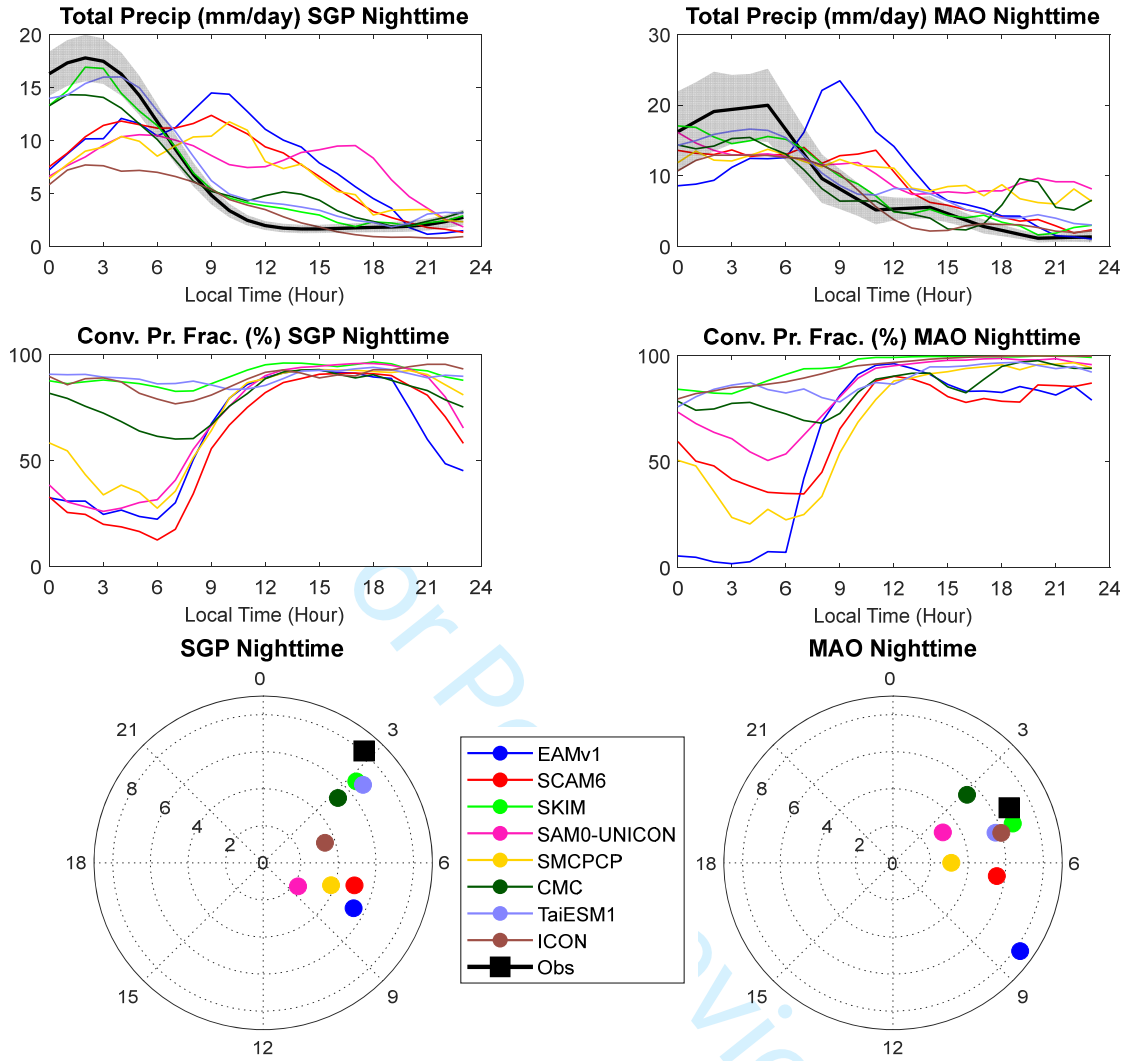
Figure 9: As in Figure 5 but for selected nocturnal precipitation days.
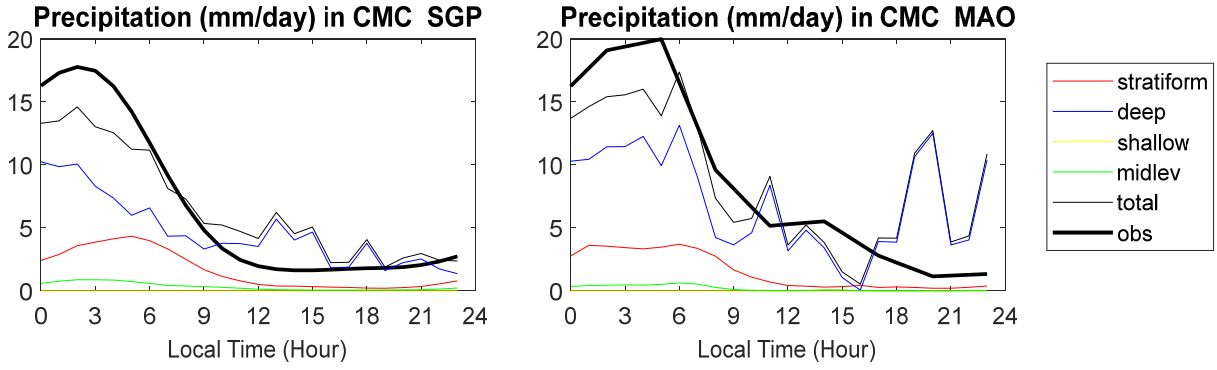
Figure 10: Precipitation rates from different components in CMC model for selected nocturnal precipitation days.
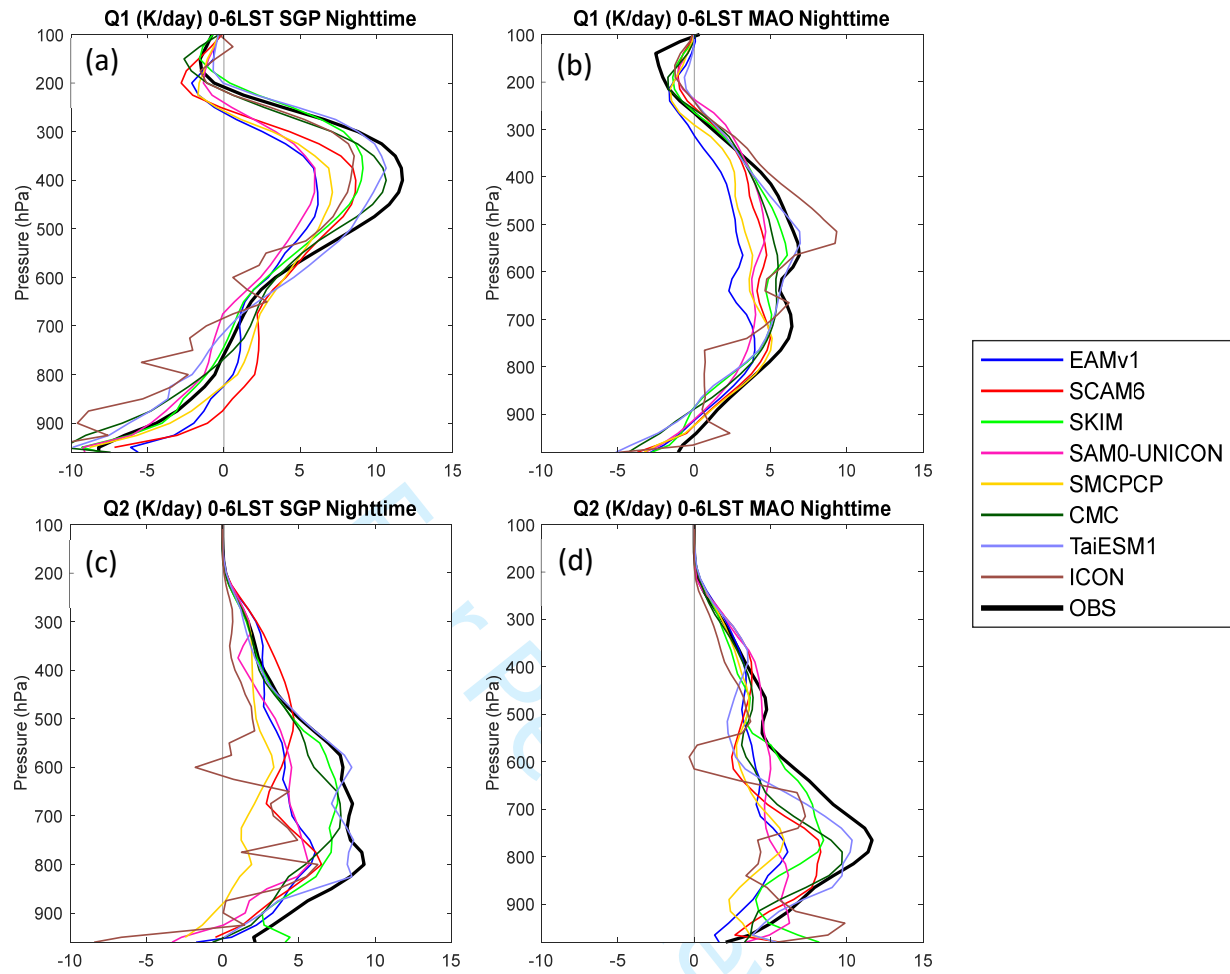
Figure 11: Q_1 and Q_2 averaged between 00 and 06 LST for selected nocturnal precipitation days at (left) SGP and (right) MAO.
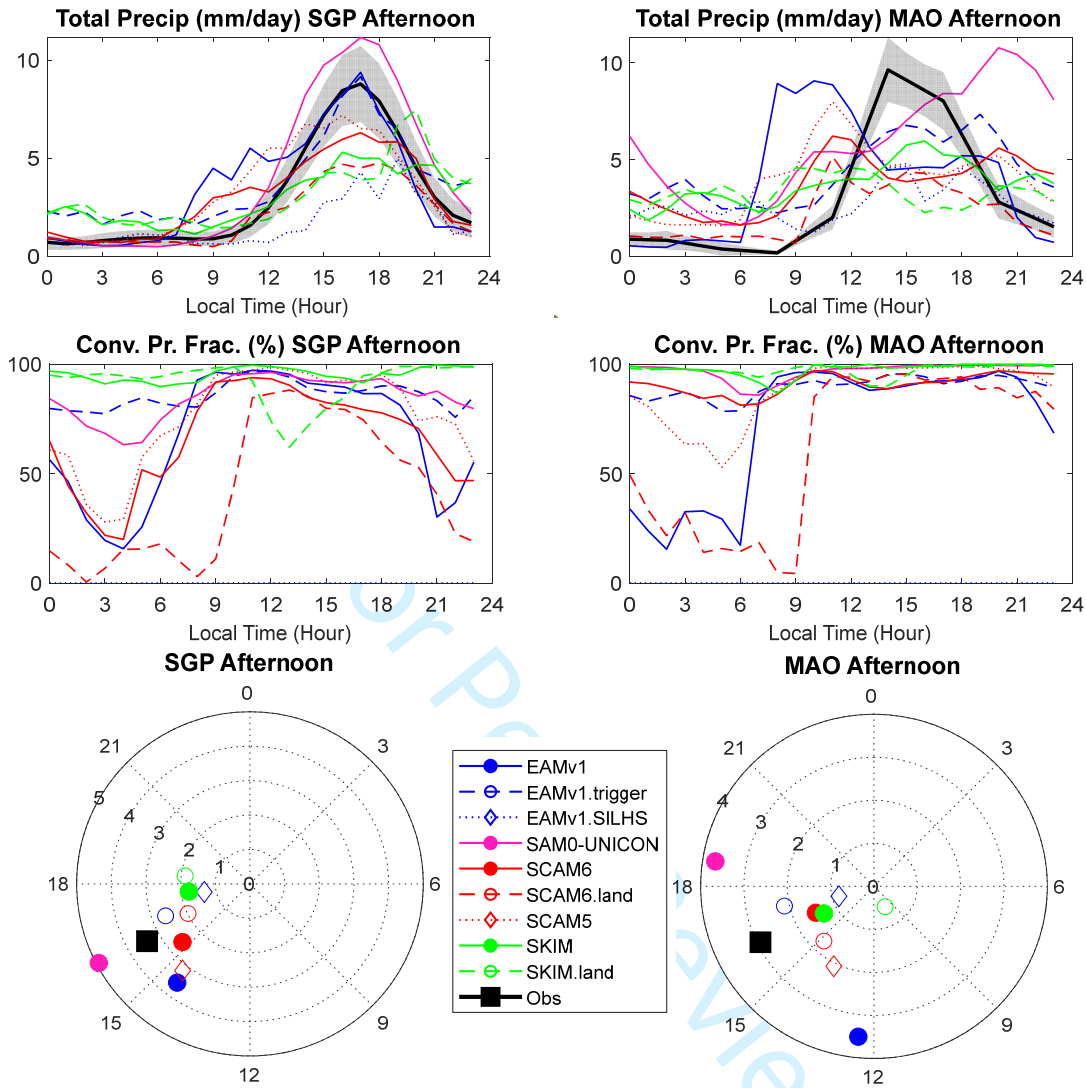
Figure 12: As in Figure 5 but for selected models/configurations for sensitivity study. Sensitivity runs are indicated by dashed/dotted lines and open symbols. Note that the convective precipitation fraction for EAMv1.SILHS (blue dotted line) is zero because the convective and large-scale precipitation is unified in CLUBB-SILHS.
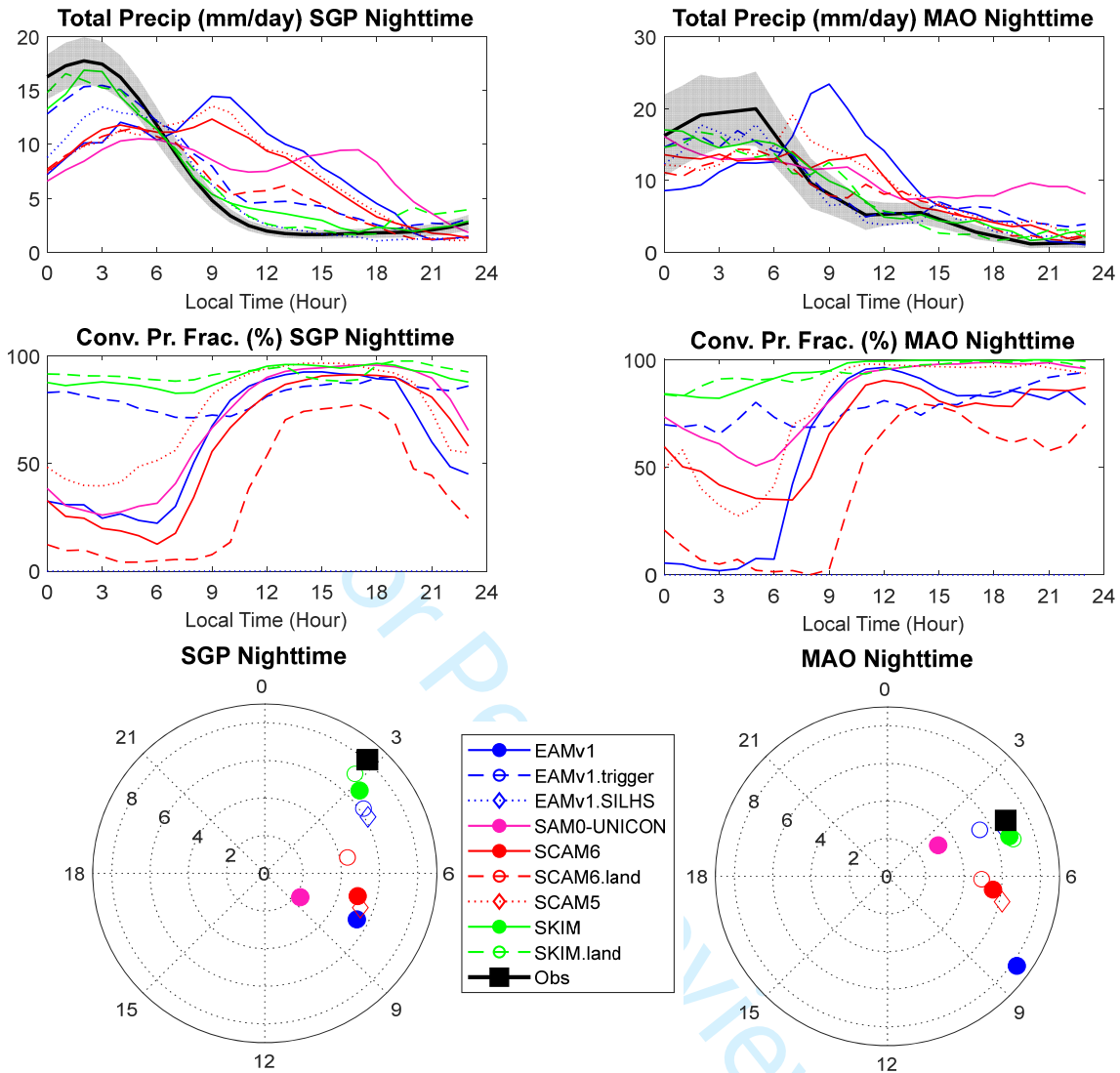
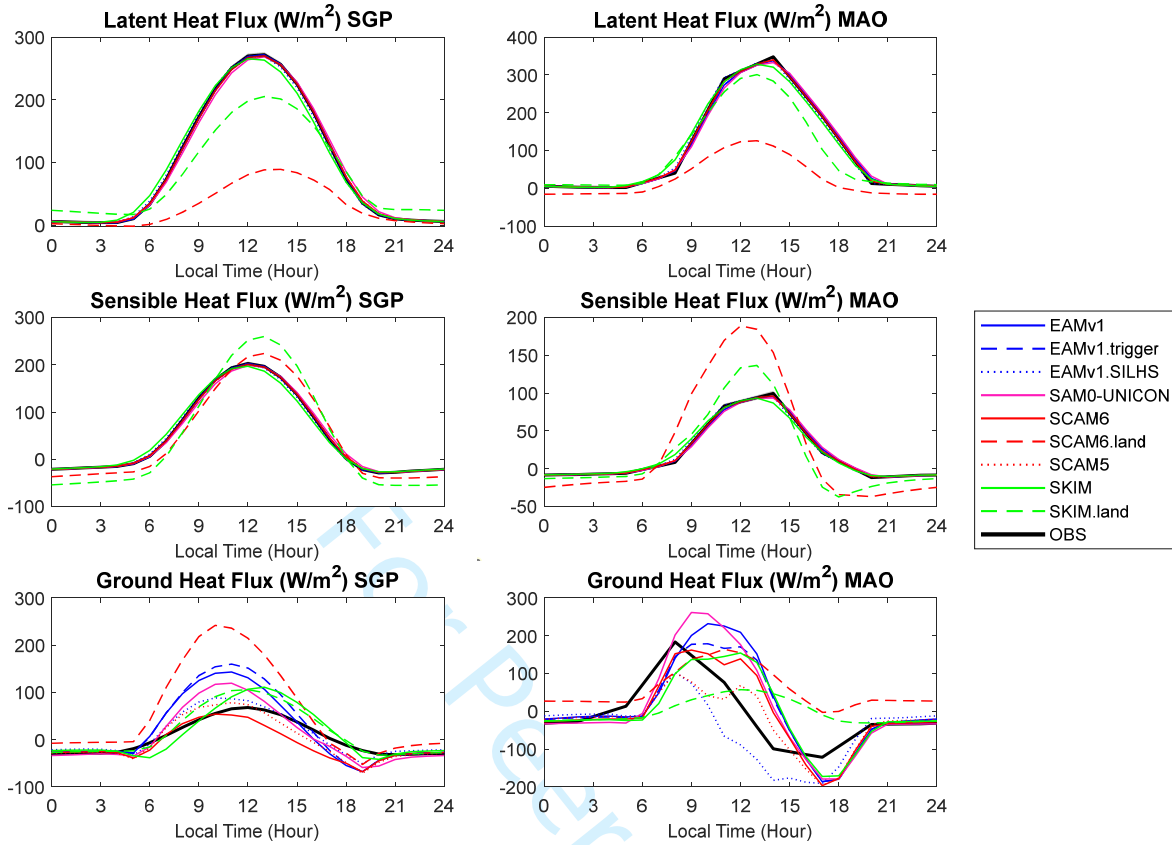Figure 13: As in Figure 12 but for nocturnal precipitation days.

Figure 14: The diurnal cycle of (top) surface latent heat, (middle) sensible heat fluxes and (bottom) ground heat flux (net radiative fluxes minus latent and sensible heat fluxes) averaged for the long-term simulation periods at (left) SGP and (right) MAO. The diurnal cycle averaged in afternoon and nocturnal precipitation days have similar performance (not shown).